Influence of TiO_2 Structure on Metal-Support Interactions in Rh/TiO_2 Catalysts Probed by Propylene Hydrogenation and Other Techniques

Hanqin Zhao[1], Li-Yin Hsiao[1], Nicholas G. Rudawski[2], Bochuan Song[1], Po-Chien Kuan[1], Lauren Hullender[1], Hagelin-Weaver[1]

[1] Department of Chemical Engineering, University of Florida, Gainesville, Florida 32611, United States

[2] Herbert Wertheim College of Engineering Research Service Centers, University of Florida, Gainesville, Florida 32611, United States

Abstract

Metal-support interactions between rhodium and nanoparticles of anatase (ANP), rutile (RNP), and brookite (BNP) TiO_2 with similar average particle sizes were investigated. The low rhodium loading (0.4 % by weight) yielded 1.5-2.0 nm Rh particles and assured maximum Rh-TiO_2 interactions. Under these closely matched conditions, the oxidation state of rhodium was shown to vary with TiO_2 structure plus particle size and reducing conditions. After reduction at 200 °C, more metallic rhodium was present at the surface of the anatase TiO_2 support with the larger particle sizes (15 nm) compared with Rh on brookite or rutile TiO_2, or smaller anatase TiO_2 nanoparticles, and this likely explains why the Rh/TiO_2-ANP is the most active catalyst in the hydrogenation of propene. A high temperature reduction (500 °C) resulted in migration of TiO_x over rhodium on anatase and brookite, but not on rutile TiO_2 supports where instead strong electronic interactions dominated. This study reveals the importance of considering TiO_2 structure and particle size, active metal particle size, as well as shape and stability of

the TiO_2 support when investigating metal-support interactions. The electronic properties of Rh depend sensitively on the TiO_2 structure, particle size and stability, and vary significantly with pretreatment conditions.

Key Words: Rh/TiO_2; Anatase, Rutile and Brookite Titania; SMSI; Propylene Hydrogenation; XPS; STEM-EELS

1. Introduction

Metal oxide supports play a significant role in the performance of heterogeneous catalysts. This is particularly true for redox active oxide supports, such as TiO_2 and CeO_2, since these materials can, in addition to simply providing a high surface area to support the active metal, also interact strongly with, and alter the electronic properties of, the active metal as well as participate in the reactions [1, 2]. Titania or TiO_2 is a particularly interesting support, and, due to its versatile properties, TiO_2 has been widely utilized in photocatalytic, electrochemical, and even in traditional industrial catalytic reactions [3-7]. TiO_2 has three main crystal structures, rutile, anatase, and brookite, among which rutile and anatase are typically the most important in catalytic applications as they tend to be more stable under reaction conditions [8]. Anatase is a better photocatalyst and has a higher surface area, but rutile is the lower energy structure and is therefore thermally more stable [9, 10]. Brookite is less common, but can be important when the TiO_2 nanoparticles have grain sizes between 5 and 30 nm [11]. In addition, the presence of metals can induce transitions between rutile, anatase, and brookite phases, and reduce (or increase) the temperature at which these transitions occur [11-13]. Thermochemical reactions utilizing TiO_2 supports are therefore complex, and, furthermore, the catalytic activity and selectivity are not only affected by the TiO_2 bulk structure, but can also depend on the TiO_2 surface structure (i.e. the surface facet exposed as well as surface defects) [14-17]. For these reasons, catalytic properties of TiO_2-supported catalysts can be very sensitive to the calcination temperature [18-20] and pretreatment conditions [21, 22]. This is further complicated by the potential to induce strong metal-support interactions (SMSIs), a signature property of TiO_2. Tauster *et al.*[5] first discovered that a high temperature (500 °C) reduction of TiO_2-supported catalysts, resulted in a drastic decrease in the CO chemisorption, and this was later shown to be due to TiO_x migration over the supported metal particles [6]. The process is at least partially reversible so most of the original metal surface area can typically be recovered by an oxidative treatment (at 400 °C) and a second low-temperature (200 °C) reduction. The TiO_x migration is often referred to as a geometric SMSI effect, since metal support interactions can, and often do, result in electronic effects also, i.e. the electronic properties of small metal particles are altered by interactions with the support, sometimes referred to as electronic metal support interactions (EMSI) [1, 23-26].

Amongst all the TiO_2-supported metal catalysts reported in the literature [27], Rh/TiO_2 is a powerful combination that has been used in several reactions ranging from steam reforming [28], reverse water gas shift and CO_2 hydrogenation [29-31] to various other hydrogenation [32-37], hydroformylation [38-41], oxidation [42-45], and photocatalytic reactions [28, 46]. Also, since the discovery of SMSIs in Pt/TiO_2 catalysts, the Rh-TiO_2 combination has been extensively investigated and a large number of studies on the effects of SMSIs on its properties have been reported [47-58]. The loss in metal surface area due to SMSIs typically decreases the catalytic activity, but the activity can increase in reactions where the metal-support interface is important, and, in addition, the selectivity to desired products can be increased by either site-blocking (i.e. poisoning of the unselective sites) or via the electronic interactions that accompanies SMSIs [1]. This is observed in various reactions over Rh/TiO_2 catalysts such as CO_2/CO hydrogenation [22, 59-62], parahydrogen induced polarization (PHIP) [63, 64], as well as in more complex hydrogenation reactions [53, 56, 65-70]. Despite all the studies of metal-TiO_2 interactions, there are still some uncertainties on the effects of TiO_2 crystal structure (anatase, rutile, and brookite) and surface termination on the induction of geometric and electronic SMSIs [71]. As mentioned, this is further complicated by the anatase-brookite-rutile transitions that can take place as the temperature is increased, transitions that can be influenced by the presence of metals, such as rhodium [72]. Several studies indicate that TiO_x migration is more facile on TiO_2 supports with a predominant anatase phase, compared with rutile TiO_2 supports [73-77]. Rutile TiO_2 has been shown to instead induce electronic metal support interactions, which leads to slightly positively charged Rh particles after reduction (higher binding energies measured with XPS compared with metallic Rh) [73]. However, there are also studies indicating that rutile induces SMSIs (TiO_x migration) while anatase does not [78], or that geometric SMSIs occur on both [79]. Other studies have revealed that the specific metal is important, since under the same conditions migration of TiO_x over Rh was shown to be more facile than over Pt, and the stoichiometry of the TiO_x layer is also dependent on the metal [80]. However, induction of SMSIs is evidently very complex, as it has also been reported that Pt enters the SMSI state more readily than Rh [81]. Surface science studies of Rh particles on thin rutile TiO_2 films with (110) surfaces have shown that encapsulation of Rh particles does occur on this surface and is more facile on defect rich TiO_2 surfaces [82, 83]. There are also indications in the literature that the exposed TiO_2 surface facet is important, and encapsulation of metal nanoparticles occur on some surface facets but not others [14, 84]. In addition, it has recently been shown that hydrocarbon gas mixtures can induce so called adsorbate-mediated geometric SMSIs [22], and there are also indications that geometric SMSIs can be induced under oxidative conditions [14]. Finally, encapsulation appears to be dependent on the TiO_2 particle size [85], as well as the size of the metal particles on the TiO_2 support [86-88]. For example, it has been shown that Au NPs of ~5 nm undergo more facile Au–TiO_2 SMSIs (migration of TiO_x over the Au nanoparticles) than those of ~2 nm and SMSIs only happens when Pt size greater than 2 nm [89]. However, this may also depend on the specific metal and the purity of the TiO_2 phase, as evidence suggests that 1.2-nm Rh particles on pure anatase TiO_2 were covered by a TiO_x layer already after reduction at 400 °C [73]. Other studies have indicated that smaller particles and single metal atoms require higher temperatures to show SMSI behavior [90]. Higher temperatures, of course, increase the potential for sintering, and noble or precious metal particles greater than 2 nm are undesirable in catalysis as a significant fraction of the metal atoms would not be available for reaction. These complications all reduce the potential for using induction of geometric SMSIs as a tool in tuning catalytic activities and selectivities [91], and it is important to understand the behavior of each system, i.e., the specific combination of active metal and support.

In this study, commercially available TiO_2 nanoparticles with highly pure rutile or anatase phases were used as supports, and the average particle size of each support was carefully selected to match, to the extent possible, the specific surface areas of the supports. Brookite nanoparticles of similar average particle size were also synthesized according to literature procedures [92]. However, matching the TiO_2 particle size is challenging since the stability of the rutile, brookite and anatase phases is dependent on the particle size, and it is important that the support is stable during reaction and various heat treatments. Therefore, a pure rutile support with the smallest possible particle size (20-50 nm) was selected (below 20 nm rutile is not the most stable phase of TiO_2). Then, an anatase support with the largest particle size (~15 nm) was selected to obtain anatase and rutile supports with similar surface areas. Larger anatase particles would have non-negligible contributions from the rutile phase, and smaller particles would have larger surface areas. Rutile TiO_2 nanorods were also synthesized and included in the study, since this support has a larger surface area than the rutile nanoparticles (i.e., closer to the anatase TiO_2). The nanorods expose a high fraction of well-defined (110) surface facets together with some (101) surfaces. A small amount of Rh (0.4% by weight) was deposited onto these supports using an incipient wetness impregnation method to examine Rh-TiO_2 interactions. Low Rh loadings were used to maximize interactions with the support and determine how the interactions are affected by the bulk and surface TiO_2 structures, while at the same time minimizing large variations in Rh particle size, which can influence these interactions. A rhodium nitrate precursor was used to avoid any effects on these catalysts caused by potential chlorine contaminations, which are difficult to avoid when using chloride precursors.

Propene hydrogenation was selected as the probe reaction, due to the low temperature of reaction over Rh/TiO_2 catalysts [93-95]. A low reaction temperature is necessary due to the potential for induction of geometric SMSIs under reducing reaction conditions at higher temperatures. This reaction is a commonly used probe reaction for olefin hydrogenations [95-100]. It is also an important reaction due to its potential in parahydrogen-induced polarization nuclear magnetic resonance applications [33, 36, 37, 63, 101, 102].

2. Experimental

2.1. Catalyst Synthesis

The following commercially available precursors and TiO_2 nanoparticles were used in the study: rhodium nitrate hydrate, $Rh(NO_3)_3 \cdot 6H_2O$ (Aldrich, 99.9%), titanium(III) chloride, $TiCl_3$ (ACROS, 99.9%), titanium(IV) chloride, $TiCl_4$ (Sigma-Aldrich, 99.9%), anatase TiO_2 nanoparticles (ANP, Nanostructured & Amorphous Material Inc., 99%, 15 nm). rutile TiO_2 nanoparticles (RNP, Nanostructured & Amorphous Material Inc., 99.8%, 20-50 nm), γ-Al_2O_3 nanoparticles (Nanostructured & Amorphous Material Inc., 99%, 11 nm), sodium hydroxide, NaOH (ACROS, 99%), urea (Fisher, 99.4%), and sodium lactate solution (Sigma-Aldrich, 60% (w/w)). Two additional anatase TiO_2 nanoparticles with smaller average particle sizes were also included (both from Nanostructured & Amorphous Material Inc., ANP10: 10 nm, 99+%, and ANP05: 5 nm, 99.8%). All commercial TiO_2 support was 350 °C calcined before the synthesis and characterization.

The rutile nanorods (RNR) were synthesized using a literature procedure [103]. In summary, 5 ml of an aqueous 15% $TiCl_3$ solution was added dropwise into a solution composed of 35 ml deionized (DI) water, 2.0 g of NaCl, and 0.663 g of NaOH. The mixture was fully dissolved and well mixed by continuous stirring in a 100-ml Teflon liner, before the Teflon liner was placed in a stainless-steel autoclave and the mixture hydrothermally treated for 24 h at 150 °C. The nanorods were recovered by centrifugation and then filtrated after cleaning by dispersing twice in DI water and ethanol, respectively, followed by drying at 105 °C overnight and calcination at 350 °C for 3 h.

The brookite nanoparticles (BNP) were also synthesized using a literature procedure [92]. First, 2.85 g $TiCl_4$ was added dropwise in DI water submerged in an ice water bath. Then, 5.0 g urea was added while maintaining constant stirring. Immediately following the urea addition, 5.0 mL sodium lactate solution (~60%) was added dropwise. The resulting mixture was then moved to a 100 mL Teflon-lined autoclave, sealed, and maintained at 200 °C for a duration of 20 hours before being naturally cooled to room temperature. The brookite nanoparticles were recovered by centrifugation and washed by dispersing first in DI water and then in ethanol, recover by centrifugation and repeating these steps twice, followed by drying at 105 °C over night and calcining in air at 500 °C for 3 h.

The Rh/TiO_2 catalysts were synthesized using the incipient wetness impregnation (IWI) method [104]. In all cases, the Rh loading was 0.4 % by weight and the catalysts are labeled according to their support, i.e., Rh/TiO_2-ANP, Rh/TiO_2-RNP, Rh/TiO_2-RNR, Rh/TiO_2-BNP. For the Rh/TiO_2-ANP and Rh/TiO_2-RNR catalysts, the Rh precursor solutions were prepared by dissolving 14 mg $Rh(NO_3)_3 \cdot 6H_2O$ in 1.0 ml of DI water and the solutions were ultrasonicated for 30 s before they were added to 1.0 g dry TiO_2 support (each) in aliquots of 200 μl at a time while stirring. In the case of the Rh/TiO_2-RNP catalyst, the same amount of Rh precursor was dissolved in 1.1 ml DI water before being added to 1.0 g support. For the Rh/TiO_2-BNP, the Rh precursor was dissolved in 628 μL of DI water and added to 1.0 g of support. The resulting mixtures were dried overnight at 80 ºC and then calcined at 350 °C for 3 h to decompose the nitrate precursor. A Rh/γ-Al_2O_3 catalyst was also synthesized using the same method with the same Rh loading and 3.2 ml DI water. It was characterized as a reference catalyst with a support that is not expected to yield strong metal support interactions.

2.2. Catalyst Characterization

2.2.1. Temperature Programmed Reduction (TPR). TPR measurements were conducted on a ChemBET 3000® instrument (Quantachrome Instruments, Inc.), using 5% H_2 balanced with N_2 as the reducing gas. Typically, the H_2-TPR experiments were performed following the BET surface area measurements. The H_2 consumption was monitored by a thermal conductivity detector (TCD) as a function of temperature using a heating rate of 10 °C/min up to the set point. The set point (maximum) temperature during the TPR experiments was either 200 °C or 500 °C, and the catalysts were kept at this temperature for one hour.

2.2.2. Specific Surface Area. Single point Brunauer Emmett Teller (BET) surface area measurements were also performed on the ChemBET 3000® instrument using 30 or 50 mg of catalyst.

Each catalyst was degassed under ultra-high purity helium gas (Airgas, Inc) at 200 ºC for 20 min. At -196 °C (immersed in liquid N_2), the N_2 molecules are deposited on the catalyst surface from the 30% N_2 gas flow (balanced with helium). The desorbing N_2 molecules are then monitored while the temperature is returned to 25 °C, and the desorbed N_2 quantified by using the known volumes of N_2 and calculating the surface area by using the cross sectional area of the nitrogen molecule (0.162 nm^2) [105].

2.2.3. X-Ray Diffraction (XRD) Analysis. XRD measurements were performed on all TiO_2-supported catalysts using a PANalytical X'Pert Powder Pro l diffractometer in Bragg-Brentano geometry. The setup was equipped with a secondary Ni filter, Cu $K_{\alpha1,2}$ radiation and an X'Celerator multi strip detector. Data were collected between 2θ angles of 20 and 80º with a time per step of 10 ms and a step size of 0.08º. Identification of observed peaks was accomplished by comparison against known standards.

The XRD data were used to calculate the crystallite or grain sizes (L) using the Scherrer equation (Equation 1). The full widths at half maximum were determined for the most intense peaks in the XRD patterns obtained from each catalyst.

Scherrer Equation:

$$L = \frac{K\lambda}{B(2\theta) * \cos(\theta)} \qquad (1)$$

K = 0.94 (Scherrer constant) [106], λ = 1.54178 [Å], 2θ is the peak position, and B is the full width of half maximum.

2.2.4. Raman Spectroscopy Analysis. Raman spectra were acquired on a LabRam ARAMIS (Horiba Jobin Yvon) spectrometer, and the measurements were carried out in the 100–1200 cm^{-1} spectral range. The samples were excited using a laser with a wavelength of 532 nm. The 10× lens objective magnification was used to focus and collect the light scattered from the samples. The emitted light was collected by a spectrograph with a grating of 1800 lines/mm.

2.2.5. CO Chemisorption Measurements. After the TPR experiments, the gas flow was switched to inert (He), and the catalysts degassed at 200 °C (after 200 °C TPR), or cooled down from 500 °C to 200 °C and then degassed for 20 minutes (after 500 °C TPR), before the catalysts were cooled down to room temperature and the CO uptake (chemisorption) was measured (also on the ChemBET 3000® instrument) using pulses of pure CO gas with known volume (84 μl).

2.2.6. Scanning/Transmission Electron Microscopy (S/TEM) Data. High-resolution transmission electron microscopy (HR-TEM) images were collected on an FEI Talos F200i S/TEM instrument at 200 kV (C_S = 1.2 mm) with beam current of ~1.2 nA using an appropriately sized objective aperture for optimal (Scherzer) HR-TEM imaging. The resulting information limit of the HR-TEM images was ~0.1 nm with all images acquired at 2k × 2k resolution using a bottom-mounted FEI Ceta 4k × 4k CMOS camera. Due primarily to mass-thickness contrast, the Rh particles appear darker compared to the TiO_2 supporting particles.

Monochromated high-angle annular dark-field scanning transmission electron microscopy (HAADF-STEM) imaging coupled with electron energy loss spectroscopy (EELS) was performed to map the distribution of anatase, rutile and brookite phases two TiO_2-supported Rh catalysts after reduction at 200 °C using a C_S probe-corrected FEI Themis Z S/TEM at 200 kV equipped with a Wein filter monochromator and Gatan Continuum ER post-column energy filter. The monochromator excitation was set to 0.8 rad with the monochromator spot number set to 12; a 0.5 μm energy selecting slit and a 30 μm probe-defining aperture were also used; under these conditions, the measured energy spread of the electrons was ~120 meV with a probe semi-angle of convergence of ~20.4 ± 0.1 mrad and a probe current of ~200 pA. For all STEM-EELS maps, a 256 nm × 256 nm area was analyzed with 1 nm step size, 1 ms dwell time, and 10 total mapping cycles; the spectrometer collection angle was 33.0 ± 0.1

mrad and the dispersion was 0.15 eV/channel to allow collection of both Ti $L_{2,3}$ and O K core-loss edges in the same electron energy loss (EEL) spectrum; the low-loss EEL spectrum (containing the zero-loss and plasmon peaks) was collected simultaneous using DualEELS mode to ensure accurate energy loss measurements and to allow removal of plural scattering effects from mapping results [107]. The aforementioned ~120 meV energy spread was verified by analyzing the zero-loss peak obtained with the monochromated STEM probe placed in vacuum and the spectrometer dispersion set to 0.015 eV/channel (not shown). Reference EEL spectra containing both the Ti $L_{2,3}$ and O K core-loss edges (with contributions from plural scattering removed) were collected from anatase, rutile and brookite standard nanoparticle samples and then the contribution of each reference spectrum to the spectra collected from the catalysts after reduction was mapped using multiple linear least squares (MLLS) fitting [108, 109].

2.2.7. Propylene Hydrogenation Experiments. 10 mg Rh/TiO_2 catalyst was diluted with 20 mg Al_2O_3 and loaded into a 0.25-inch quartz reactor tube. Prior to reaction experiments, the catalyst was pretreated by heating to 200 °C at a rate of 10 °C/min under 5% H_2 at 100 standard cm^3/min (sccm). The catalyst was kept under the reducing flow at 200 °C for one hour before the reactor was cooled down to room temperature under inert flow (He at a 95 sccm). These catalysts are denoted as 200R. The propylene (C_3H_6) hydrogenation activity was evaluated as a function of temperature between 25 and 150 °C using the following flow rates: C_3H_6: 2 standard cm^3/min (sccm), H_2: 2 sccm, N_2: 3 sccm, and He: 91 sccm. The products were analyzed by an on-line Agilent 6890N gas chromatograph (GC) equipped with a TCD. The propylene conversion was calculated using Equation 2, where $F_{C_3H_6}$ is the measured volumetric flowrate of propylene, determined by taking the average of three sample injections.

$$X_{C_3H_6} = \frac{F_{C_3H_6,in} - F_{C_3H_6,out}}{F_{C_3H_6,in}} \cdot 100\ [\%] \qquad (2)$$

In a second set of experiments a fresh catalyst was loaded into the reactor (10 mg of Rh/TiO_2, diluted with 20 mg Al_2O_3) and reduced at 500 °C before the propylene hydrogenation activity was measured as a function of temperature. These catalysts are denoted 500R. Reaction activities were then remeasured on same catalyst bed after oxidation at 400 °C and another reduction at 200 °C (catalysts labeled 200RR).

2.2.8. X-Ray Photoelectron Spectroscopy (XPS) Measurements. XPS data were collected on an ULVAC-PHI XPS instrument using a 100 μm scan area and 25W x-ray power. The powder catalysts were mounted on the sample holder using double-sided tape. To avoid differential charging, a low energy electron flood gun and the ion gun were set to neutralization mode. The survey spectra were collected with a pass energy of 187.85 eV and 10 scans total. Elemental compositions were obtained from the survey spectra using standard atomic sensitivity factors for each peak. For the Rh 3d peaks 25 scans were collected with a pass energy of 46.95 eV. All other high-resolution peaks (C 1s, O 1s and Ti 2p) were collected with a pass energy of 23.5eV and 5 scans. The XPS data processing included a Shirley background subtraction and an 11-point 2^{nd} order Savitsky-Golay smoothing routine. The narrow scans were also normalized to facilitate identification of differences in oxidation states between elements on the different catalysts.

3. Results and Discussion

The fresh catalysts consist of Rh_2O_3 (or RhO_y where $y \leq 1.5$) supported on TiO_2 and must be reduced to Rh/TiO_2 before reaction. Therefore, the RhO_y/TiO_2 catalysts were characterized in detail as a function of reduction treatment to determine the effects of the TiO_2 structure on the reducibility of these catalysts. Two reduction temperatures (200 °C and 500 °C) were selected as it is well known that strong metal support interactions leading to migration of TiO_x over metal nanoparticles are induced at 500 °C but not at 200 °C (and 200 °C is often needed to assure that the active metal is indeed metallic) [5].

Since migration of TiO_x has been shown to be reversible by a 400 °C oxidation treatment, catalysts reduced at 500 °C were reoxidized at 400 °C and then reduced a second time at 200 °C. The effects of these reduction-oxidation (redox) treatments on the hydrogenation of alkenes were evaluated using ethylene and propylene as probe reactants. A Rh/γ-Al_2O_3 catalyst synthesized using the same method was added for comparison (see Supporting Information) to include a support which is not expected to yield strong metal-support interactions.

3.1. XRD Measurements

To confirm that the different reductive treatments do not alter the crystal structure, i.e., the anatase, rutile, and brookite phases, of the supports, X-ray diffraction (XRD) patterns were obtained from the catalysts after the different treatments (as well as from the bare supports) as shown in Figure 1. The average crystallite sizes of these phases were also determined using the Scherrer equation after the different redox treatments (Table 1). The commercial anatase and rutile nanoparticles together with the as-synthesized brookite nanoparticles and rutile nanorods do exhibit strong features due to the expected phases in the XRD patterns (Figure 1). However, a minor rutile phase is observed in the anatase support, i.e. the XRD patterns obtained from the ANP support have a small contribution from the rutile phase, Figure 1(a). As mentioned, the stability of the anatase, rutile, and brookite phases of TiO_2 exhibit a particle size dependence and anatase is the most stable phase in small nanoparticles (below 10 nm), rutile is the stable bulk structure, and brookite is stable in an intermediate particle size range (*vide infra*) [110]. Therefore, it is very difficult to match the specific surface areas of TiO_2 supports with different crystal phases. Since the rutile phase is minor and is not further altered by the redox treatments, we chose to work with the 15-nm anatase support. No other phases can be detected in XRD patterns obtained from the ANP-, RNP-, BNP- supported catalysts after catalyst synthesis and the different reduction and oxidation treatments (Figure 1(a-c)). Even in the case of rhodium supported on brookite TiO_2, which has been shown to transform into anatase TiO_2 during reduction at 500 °C [111], no phase other than brookite is observed in the current study (Figure 1(c)). Furthermore, the average crystallite sizes of the commercial TiO_2 supports (TiO_2-ANP and TiO_2-RNP) are not altered significantly with Rh addition and different redox treatments (Table 1). A slight increase in the brookite crystallite size is observed after Rh addition, but no further growth is detected after the different redox treatments (Table 1).

The TiO_2 nanorods also consist of the rutile phase before catalyst synthesis, with other phases, if present, being within the noise level (Figure 1(d)). However, after addition of Rh (impregnation with rhodium nitrate) and calcination at 350 °C, peaks due to a brookite phase are introduced in the XRD pattern obtained from the Rh/TiO_2-RNR catalyst revealing that a brookite phase has formed. This is unexpected, since rutile is the more stable and therefore thermodynamically favored phase of TiO_2. It appears that the brookite phase is induced by the catalyst synthesis procedure, i.e., during impregnation with rhodium nitrate or the subsequent calcination at 350 °C. To determine if the transformation is due to the incipient wetness impregnation method, if rhodium is necessary, and if this is specific for Rh/TiO_2, a few additional catalysts were synthesized, a lower loading (0.15% Rh) Rh/TiO_2 catalyst, an IrO_2/TiO_2 via urea precipitation and a Pt/TiO_2 using the incipient wetness impregnation method. The XRD patterns obtained from these catalysts are provided in Figure S1(a). A simulated incipient wetness impregnation was also performed, where the rutile nanorods were dispersed in an aqueous solution containing the same amount of nitrate ions as the rhodium precursor solution, but without rhodium ions. It appears that rhodium in the solution is necessary for brookite formation, as no brookite peaks can be detected after the simulated IWI treatment (Figure S1(b)). More brookite is introduced by the incipient wetness impregnation compared with the precipitation method, although quantifying the amount (%) of brookite in the samples is challenging due to the poor crystallinity of this phase (Figure S1(a)). Finally, temperature programmed reduction of the rutile TiO_2 nanorods without added Rh does not induce brookite formation regardless of the final temperature (200 or 500 °C), as shown in Figure S1(b). Since brookite was not observed on the commercial rutile TiO_2 nanoparticles and is typically only reported for anatase supports, i.e. anatase may transform into brookite upon heating before the more stable rutile phase forms [13, 43], the crystallite size of the TiO_2 rods and potentially the stability of the surface facets exposed together with the presence of rhodium ions are likely important for the transition. It has been shown that brookite is the more stable phase for nanoparticles in certain intermediate size ranges, and while the specific crystallite size range varies somewhat between reports, the lower bound for brookite is 5-11 nm while the upper bound is between 20 and 35 nm [8, 11, 110]. The crystallite sizes of the rutile TiO_2 nanorods fall in this range (Table 1). It is interesting to note that the peaks due to the brookite phase are more intense for the 0.15% Rh compared with the 0.4% Rh loadings. Despite the introduction of a brookite phase, the average crystallite size of the rutile phase is increased slightly during catalyst synthesis, i.e., after adding Rh (Table 1). No further changes in the XRD patterns are observed after the various redox treatments (Figure 1(d)) and the crystallite sizes calculated by Scherrer Equation [106] are not altered significantly (Table 1).

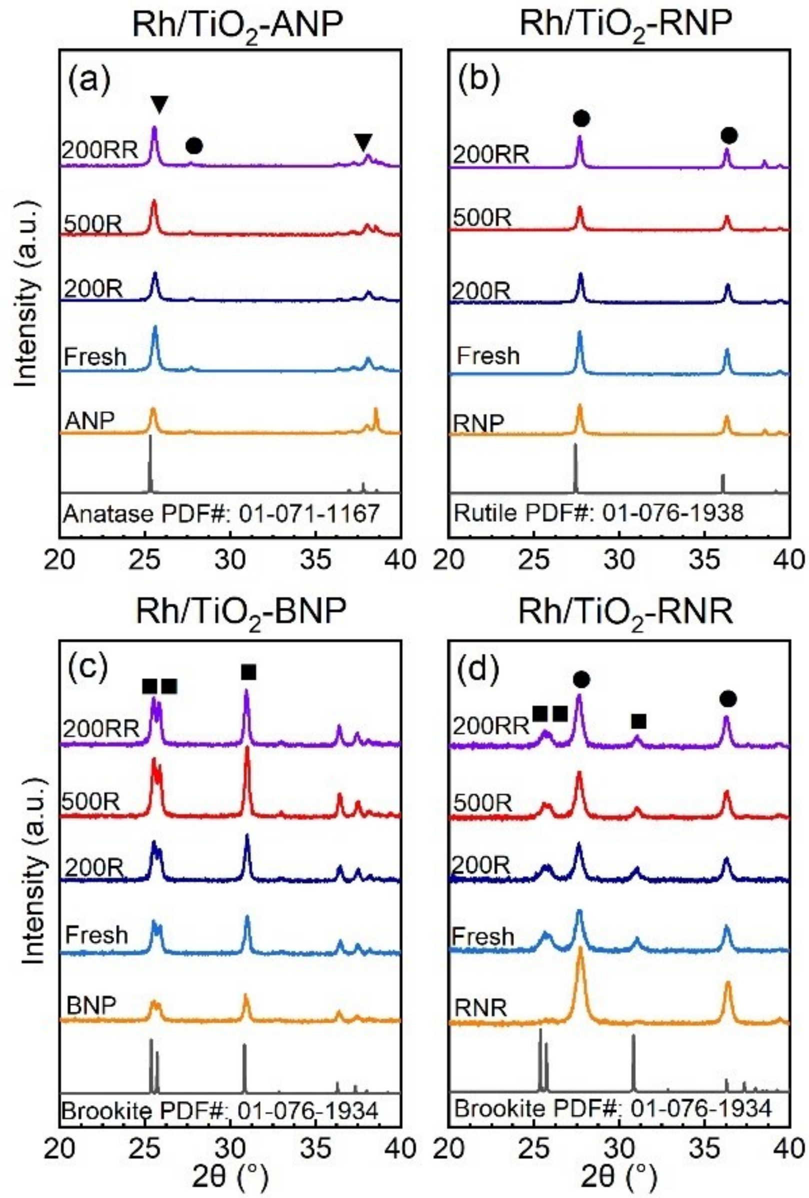

Figure 1. X-ray Diffraction (XRD) patterns obtained from (a) Rh/TiO_2-ANP, (b) Rh/TiO_2-RNP, (c) Rh/TiO_2-BNP, and (d) Rh/TiO_2-RNR following TPR to 200 °C (200R), TPR to 500 °C (500R), and TPR to 500 °C followed by oxidation at 400 °C and re-reduction at 200 °C (200RR). Symbols indicate peak positions of reference anatase: ▼, brookite: ■, and rutile: ● phases.

Table 1. Crystal structures and grain sizes calculated from the XRD data using the Scherrer equation for the TiO_2 supports and Rh catalysts before and after different reduction-oxidation treatments.

Sample	Pretreatment [a]	Main (Minor) Crystal Phase	Grain Size of Main Phase [nm] [b]	Grain Size of Minor Phase [nm] [c]
TiO_2-ANP	Fresh	Anatase	25.6	-
Rh/TiO_2-ANP	Fresh	Anatase	26.2	-
Rh/TiO_2-ANP	200R	Anatase	24.3	-
Rh/TiO_2-ANP	500R	Anatase	26.7	-
Rh/TiO_2-ANP	200RR	Anatase	24.7	-
TiO_2-RNP	Fresh	Rutile	31.0	-
Rh/TiO_2-RNP	Fresh	Rutile	32.3	-
Rh/TiO_2-RNP	200R	Rutile	33.2	-
Rh/TiO_2-RNP	500R	Rutile	34.0	-
Rh/TiO_2-RNP	200RR	Rutile	32.8	-
TiO_2-BNP	Fresh	Brookite	29.7	-
Rh/TiO_2-BNP	Fresh	Brookite	32.1	-
Rh/TiO_2-BNP	200R	Brookite	34.8	-
Rh/TiO_2-BNP	500R	Brookite	33.1	-
Rh/TiO_2-BNP	200RR	Brookite	33.3	-
TiO_2-RNR	Fresh	Rutile	15.5	-
Rh/TiO_2-RNR	Fresh	Rutile (Brookite)	19.1	16.6
Rh/TiO_2-RNR	200R	Rutile (Brookite)	20.1	20.4
Rh/TiO_2-RNR	500R	Rutile (Brookite)	20.0	17.2
Rh/TiO_2-RNR	200RR	Rutile (Brookite)	20.9	18.9

[a] Pretreatment: Fresh: catalyst after calcination at 350 °C for four hours, 200R: catalyst after TPR measurement up to 200 °C, 500R: catalyst after TPR measurement up to 500 °C, 200RR: TPR up to 500 °C followed by oxidation at 400 °C and re-reduction at 200 °C.

[b] Calculated using the Scherrer equation by averaging the crystallite sizes obtained from the (25.3, 37.0, 37.8, 38.6) peaks of the anatase phase and the (27.4, 36.1, 39.2) peaks of the rutile phase.

[c] Calculated using the Scherrer equation and the (25.4, 25.7, 30.8, 36.3) peaks of the brookite phase.

3.2. Raman Spectroscopy

Since XRD can only detect crystalline phases with sufficient long-range order, selected supports and catalysts were also evaluated using Raman Spectroscopy, since some phases can be detected at lower concentrations in the Raman spectra compared with XRD [112, 113].

3.2.1. Anatase Titania Nanoparticles and Catalysts. The peaks in the Raman spectra obtained from the TiO_2-ANP support and the Rh/TiO_2-ANP catalysts after reduction at 200 and 500 °C are consistent with the anatase phase of TiO_2 [114, 115]. More specifically, the observed peaks are assigned to the following vibrational modes: E_g (144 and 197 cm^{-1}), B_{1g} (399 cm^{-1}), A_{1g}/B_{1g} (513,519 cm^{-1}), and E_g (639 cm^{-1}) of the anatase phase [115, 116]. The E_g modes at 144 and 197 cm^{-1} are shifted to slightly higher wavenumber after reduction, and while this shifts the most intense peak towards the peak location of brookite TiO_2, no other peaks due to brookite are observed (Figure 2(a)). Furthermore, this blueshift has been observed previously under reducing conditions and has been assigned to the introduction of oxygen vacancies in the TiO_2 [114, 115, 117-120]. It is also evident in Figure 2(a) that the stretching modes (E_g) of the vibrations are more susceptible to oxygen vacancies and TiO_2 particle size effects (phonon confinement) than the bending modes (A_{1g} and B_{1g}), which is consistent with literature [115, 121]. Particle size effects with increasing temperature would lead to redshifts according to literature [114]. This suggests, in accordance with the XRD data, that the TiO_2-ANP crystallite sizes in the current study do not increase significantly with increasing reduction temperature. No peaks due to rutile TiO_2 can be detected in the Raman spectrum obtained from the TiO_2-ANP support and catalysts.

3.2.2. Rutile Titania Nanoparticles and Catalysts. The Raman spectra obtained from the TiO_2-RNP support, are also consistent with the vibrational modes observed in the rutile TiO_2 phase, B_{1g} (143 cm^{-1}), E_g (447 cm^{-1}), A_{1g} (612 cm^{-1}) and E_g (639 cm^{-1}) [115, 122]. Unfortunately, the weak B_{1g} mode of rutile TiO_2 at 143 cm^{-1} overlaps with the main E_g peak of anatase, so ruling out the presence of a small anatase impurity in the rutile support is not possible from the Raman data. The feature at 240 cm^{-1} is due to second order scattering effects [122, 123]. Distinct peak shifts in the rutile Raman features are observed after reduction at 200 and 500 °C for the Rh/TiO_2-RNP catalysts, particularly for the E_g mode at 447 cm^{-1} (Figure 2(b)). This is consistent with the reduction of TiO_2 (decreasing O/Ti ratio) as reported in literature [124, 125], although introduction of oxygen vacancies does not always result in peak shifts [126].

3.2.3. Brookite Titania Nanoparticles and Catalysts. The brookite phase of TiO_2 has a large number of Raman active modes [127-129]. The Raman spectra obtained from the TiO_2-BNP nanoparticles and the Rh/TiO_2-BNP catalysts are consistent with the brookite phase (Figure 2(c)). Although there is overlap between some peaks, the main features in the Raman spectra of Figure 2c are due to eight A_{1g} vibration modes (at 125, 152, 194, 246, 412, 492, 545, and 640 cm^{-1}), three B_{1g} modes at 212, 283 and 327 cm^{-1}, four B_{2g} modes at 325, 366, 460 and 584 cm^{-1} and two B_{3g} modes at 318 and 500 cm^{-1} [127, 128]. All peaks observed in the Raman spectra obtained from the TiO_2-BNP support and catalysts can be identified as originating from the brookite phase of TiO_2, and no major changes are observed in the Raman spectra obtained from the Rh/TiO_2-BNP catalysts after reduction at 200 and 500 °C (Figure 2(c)). Some broadening of the peaks is observed, which makes it difficult to determine if a small amount of anatase is present in the Rh/TiO_2-BNP catalysts (as the main vibrational mode of anatase at 144 cm^{-1} is located between the 125 and 152 modes of brookite TiO_2).

3.2.4. Rutile Titania Nanorods and Catalysts. As expected, the Raman spectrum obtained from the rutile TiO_2 nanorods (RNR) is consistent with the rutile phase of TiO_2 (Figure 2(d)). If present, features due to anatase and brookite are within the noise level. The main difference between the Raman spectra obtained from the TiO_2-RNP and TiO_2-RNR supports is the relative intensity of the peaks, but this is likely due to differences in particle size or shape of the TiO_2 [123, 130]. After catalyst synthesis and reduction at 200 °C, it is evident that the main peak of the brookite TiO_2 phase is present in the Raman spectrum obtained from this catalyst (Figure 2(d)). After reduction at 500 °C, the contribution from brookite TiO_2 has increased even though the XRD data did not indicate a significant difference in brookite content between the two reduction temperatures. As mentioned, due to overlapping brookite TiO_2 peaks, it is not possible to rule out the presence of a small poorly crystalline anatase phase.

The Raman data obtained from the Rh/TiO_2 catalysts confirm that the main phases are those expected, and that, if present, the contributions from other phases are small, except for the Rh/TiO_2-RNR catalysts.

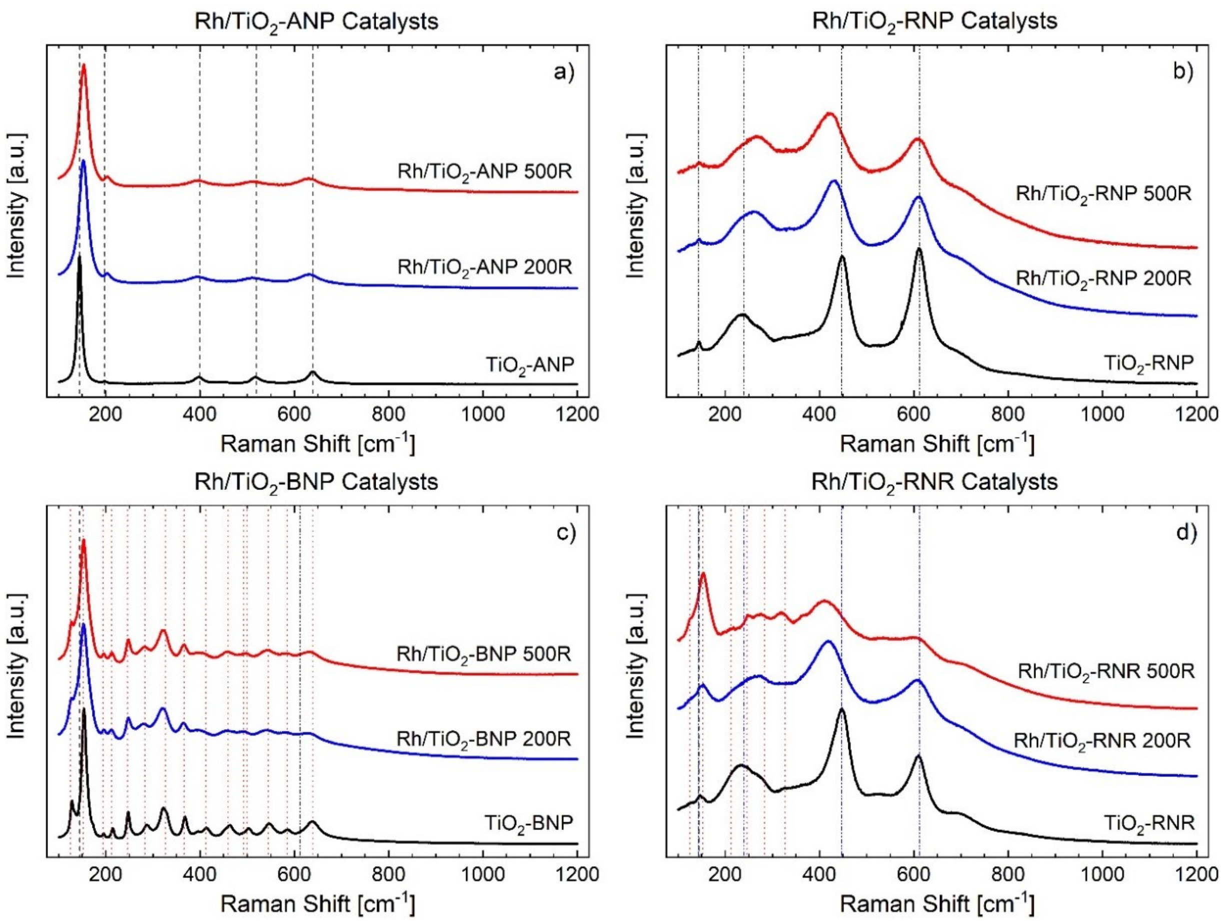

Figure 2. Raman data obtained from the different TiO_2 supports and Rh/TiO_2 catalysts after 200 °C (200R) or 500 °C (500R) reduction. (a) TiO_2-ANP support and Rh/TiO_2-ANP catalyst, (b) TiO_2-RNP and Rh/TiO_2-RNP, (c) TiO_2-BNP and Rh/TiO_2-BNP, and (d) TiO_2-RNR and Rh/TiO_2-RNR. Dashed black lines: Raman peaks due to the anatase TiO_2 phase, dash-dot-dot blue lines: peaks due to rutile TiO_2, and dotted red lines: peaks due to brookite TiO_2.

3.3. Temperature Programmed Reduction

The hydrogen uptake was monitored during temperature programmed reduction (10 ºC/min) up to 200 ºC (TPR-200) and 500 ºC (TPR-500). As mentioned, reduction at 200 ºC will primarily reduce the metal oxide (RhO_y) nanoparticles on the fresh catalysts, while reduction at 500 ºC is expected to also result in reduction of the TiO_2 surface. Therefore, a large difference in hydrogen uptake during reduction up to 500 ºC versus reduction up to 200 ºC is typically indicative of significant hydrogen spillover onto the oxide support (TiO_2) at the higher reduction temperature [131]. However, this is oversimplified, and it is evident that the reducibility of the fresh RhO_y/TiO_2 catalysts is very dependent on the structure, and potentially also the shape, of the TiO_2 support (Figure 3). These differences will be discussed in detail below. For comparison, a Rh/γ-Al_2O_3 catalyst and the two Rh/TiO_2 catalysts with smaller anatase particle sizes (TiO_2-ANP05 and TiO_2-ANP10) have been included in Supporting Information for comparisons (Figure S2).

3.3.1. Rhodium on Anatase Titania Nanoparticles. The reduction of the Rh/TiO_2-ANP catalyst during TPR-200 results in a sharp peak at 145 ºC, indicating reduction of RhO_y to Rh metal (Figure 3(a)). Only a small shoulder, and thus minor hydrogen uptake, is observed in the TPR spectrum once the temperature has reached 200 ºC, indicating little hydrogen spillover at this temperature. It is evident from the TPR-500 data that the anatase TiO_2 support requires temperatures above 400 ºC for reduction (Figure 3(a)), and a significantly higher hydrogen uptake is observed during reduction at 500 ºC (Table S1). This indicates significant hydrogen spillover onto the support with concomitant reduction of the TiO_2. After reoxidation of the TPR-500 catalyst, it appears that the first peak is more intense and has shifted from 145 °C to 122 °C, but the hydrogen consumption is similar to the original uptake (Figure 3 and Table S1). These observations suggest a small increase in rhodium particle size and perhaps removal (restructuring) of species that interact closely with the support.

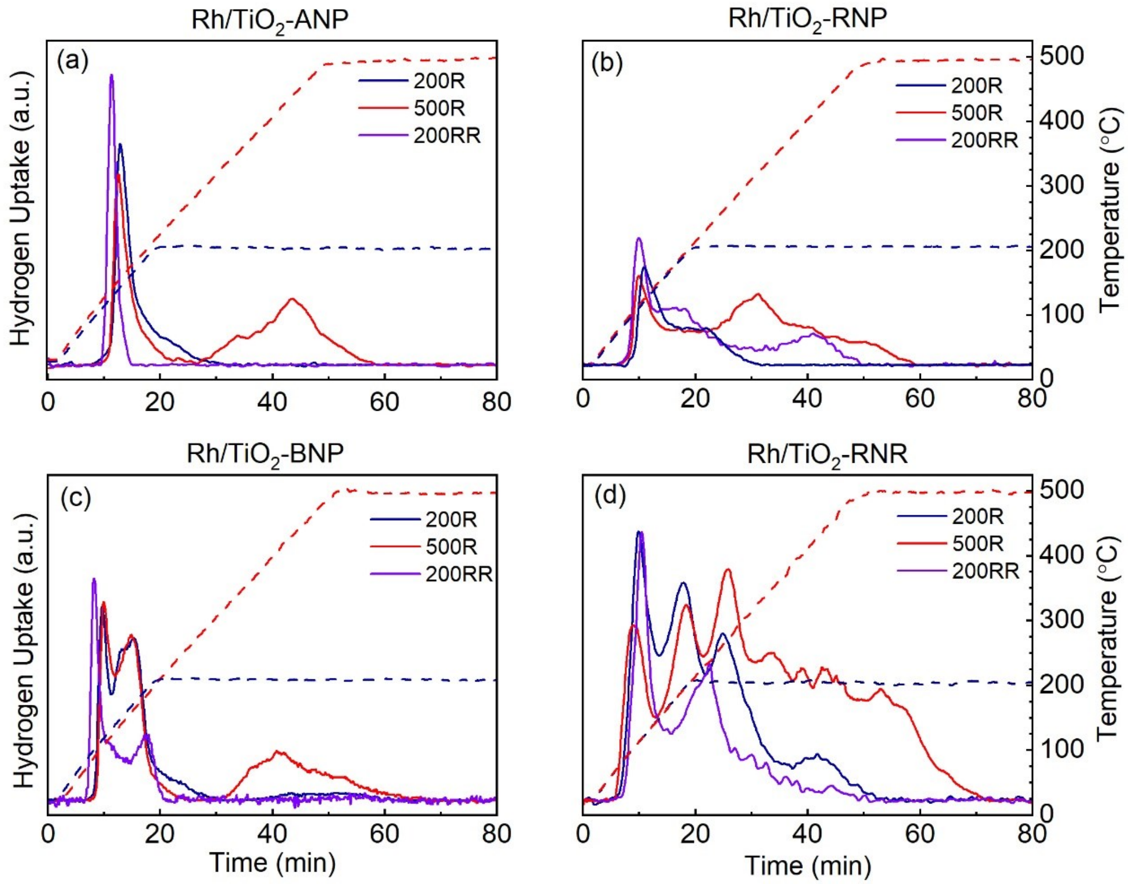

Figure 3. Temperature program reduction using 5% H_2 (H_2-TPR) spectrum for (a) Rh/TiO_2-ANP, (b) Rh/TiO_2-RNP, (c) Rh/TiO_2-BNP, and (d) Rh/TiO_2-RNR with 10 °C/min heating rate. Labels are TPR to 200 °C (200R, blue), TPR to 500 °C (500R, red), and TPR up to 500 °C followed by oxidation at 400 °C and re-reduction at 200 °C (200RR, purple). Red and blue dashed lines denote the temperature profiles. All data are plotted on the same scale.

3.3.2. Rhodium on Rutile Titania Nanoparticles. The reduction of the RhO_y on the fresh Rh/TiO_2-RNP catalyst is initiated at a lower temperature (122 ºC, Table S1) than on the fresh Rh/TiO_2-ANP catalyst. However, the reduction is much slower, as evidenced in the broader peak compared with the Rh/TiO_2-ANP catalyst, and the hydrogen uptake continues after the temperature reaches 200 ºC. While lower RhO_y reduction temperatures have been observed for catalysts supported on rutile TiO_2 compared with anatase-supported catalysts [132], comparisons are challenging, at best, since the position of the first TPR peak is very dependent on the initial metal oxide, i.e. RhO_y, particle size, and thus also on the active metal loading, on the support [46]. Therefore, since the metal dispersions are often very different between anatase and rutile TiO_2 supports, the opposite trend has also been reported [44, 133]. It is possible that the interactions between RhO_y and rutile TiO_2 are very dependent on particle size, such that smaller RhO_y particles are more difficult to reduce (due to strong interactions between Rh and rutile TiO_2), while slightly larger particles are easier to reduce on rutile- compared with anatase-supported catalysts [73, 134, 135]. It is also possible that some hydrogen spillover onto the rutile TiO_2 support occurs already at this temperature (200 °C), and this is causing the slow hydrogen uptake. More hydrogen spillover at lower temperatures on rutile compared with anatase TiO_2 has been observed over Ni/TiO_2 catalyst [136], and reduction of Ti^{4+} to Ti^{3+} has been reported at 200 °C on Pd catalysts supported on rutile TiO_2 [137]. A higher number of oxygen vacancies (or hydroxyl groups) on rutile TiO_2 (compared with anatase TiO_2) has also been observed on Ru/TiO_2 catalysts [133], and this is consistent with more facile formation of surface oxygen vacancies on rutile compared with anatase TiO_2 supports, despite the higher thermal stability of rutile TiO_2 [136].

The TPR-500 data reveal that the reduction of the rutile TiO_2 nanoparticles is different compared with the anatase TiO_2 nanoparticles. The hydrogen uptake window over the Rh/TiO_2-RNP catalyst is large and continues from the first peak up to 500 °C. Therefore, the hydrogen consumption during 500-TPR is higher than during the 200-TPR, as for the Rh/TiO_2-ANP catalyst, but the peak from the Rh/TiO_2-RNP catalyst is broader and the peak maximum appears at a lower temperature (320 versus 440 °C). These observations are consistent with a slower reduction rate of rutile TiO_2, but the total uptake is surprising as the total hydrogen consumption during 500-TPR is expected to be much larger from the anatase-supported catalyst due to more facile formation of bulk oxygen vacancies in anatase compared with rutile TiO_2 [137, 138]. Of course, due to the slow hydrogen uptake, quantification is more difficult and the uncertainty in the measured hydrogen consumption at higher temperatures is larger for the Rh/TiO_2-RNP catalyst compared with the ANP-supported catalyst.

After oxidation at 400 °C (following the 500 °C TPR) only a slight shift in the first reduction peak to lower temperatures (113 °C) compared with the original 200R data is observed in the TPR curve. The shift to lower reduction temperatures is much larger for the Rh/TiO_2-ANP catalyst which suggests that the Rh on the surface of the rutile TiO_2 support is more resistant to sintering. This is further evidence that the interactions between Rh and TiO_2 are dependent on the phase of the titania, i.e., anatase versus rutile [78, 139, 140].

3.3.3. Rhodium on Brookite Titania Nanoparticles. On the brookite support, reduction of RhO_y is observed at 120 °C, similar to the rutile TiO_2 support. However, the similarities with the Rh/TiO_2-RNP end there. In the TPR spectrum obtained from the Rh/TiO_2-BNP catalyst a second distinct feature is also observed at 165 °C. The total hydrogen uptake on this catalyst during TPR-200 is close to the hydrogen consumed during TPR-500 for the Rh/TiO_2 catalysts support on ANP and RNP TiO_2, indicating significant hydrogen spillover on the brookite TiO_2 even at this low temperature (below 200 °C). Additional hydrogen is consumed during reduction at 500 °C, and the peak maximum at 415 ºC is closer to that observed over the Rh/TiO_2-ANP catalysts.

After reduction at 500 °C and reoxidation at 400 °C, the first peak is shifted to slightly lower temperatures (100 °C), similar to the behavior of the Rh/TiO_2-ANP catalyst. It appears that significant restructuring occurs during the high temperature reduction or reoxidation, as the second peak is smaller and has shifted to slightly higher temperatures. This suggests that the redox treatment results in Rh particle size growth with less efficient hydrogen spillover onto the titania support.

3.3.4. Rhodium on Rutile Titania Nanorods. The Rh/TiO_2-RNR catalyst exhibits a very different behavior compared with the Rh supported on the ANP and RNP supports. Three distinct peaks are observed in the TPR-200 and TPR-500 data obtained from this catalyst suggesting that there are at least three different types of reducible species on this catalyst. The initial peak at 112 °C is consistent with RhO_y reduction on the TiO_2-RNR support, and the peak location is closer to that observed on the TiO_2-BNP support than on the rutile TiO_2 nanoparticles. The second peak is located just below 195 °C, while the third peak appears above 200 °C (272 °C according to the TPR-500 data). Considering the high intensity of the first peak, it is likely that the second peak is due to reduction of TiO_2. This peak may be due to reduction of the brookite TiO_2 phase that was introduced during catalyst synthesis. While the corresponding peak is observed at a lower temperature on the pure TiO_2-BNP support, this could be due to particle size differences (both RhO_y particle and TiO_2-BNP crystallite sizes). The hydrogen uptake over the Rh/TiO_2-RNR catalyst during TPR up to 200 °C is significantly higher than the hydrogen consumed by any of the other TiO_2-supported catalysts (ANP, RNP and BNP) during TPR up to 500 °C (Table S1). This is likely due to the presence of two TiO_2 phases, the higher specific surface area, and a higher number of defects on the TiO_2 nanorods compared with the other TiO_2 supports.

The hydrogen uptake over the Rh/TiO_2-RNR catalyst continues above 200 °C, so the hydrogen consumed by the RNR-supported catalysts during TPR up to 500 °C is very large. The third peak, also associated with TiO_2 reduction, is closer to the peak obtained from the Rh/TiO_2-RNP catalyst (320 °C) than the peak from the Rh/TiO_2-ANP catalyst (440 °C) but is larger and sharper compared with the data from either of the other catalysts. These observations suggest strong electronic metal-support interactions on the Rh/TiO_2-RNR catalyst which facilitates hydrogen spillover but also likely indicate that the rutile TiO_2 nanorods are less stable under reducing conditions compared with the other TiO_2 supports. The differences in the TPR data obtained from the Rh/TiO_2-RNP and Rh/TiO_2-RNR catalysts also suggest that the reducibility of these catalysts is not only dependent on the bulk but also the surface structure of the TiO_2 support (including defects), and is potentially affected by different Rh nanoparticle sizes [141, 142].

A significant restructuring during reduction and reoxidation is also observed over the Rh/TiO_2-RNR catalyst. After the redox treatment, only two distinct peaks are observed and both peaks are shifted to slightly higher temperatures. In fact, the shape of the TPR spectrum obtained from the Rh/TiO_2-RNR catalyst is very similar to that obtained from the Rh/TiO_2-BNP catalyst, suggesting that the reduction behavior of this catalyst is dominated by the brookite phase.

3.4. Specific Surface Area Measurements

To determine if significant sintering (particle growth) of the TiO_2 supports occurred during the different redox treatments, BET surface area measurements were performed on all catalysts after the different redox treatments (Table 2). The specific surface areas of the bare supports (after calcination at 350 °C) are also included. After catalyst synthesis (introduction of Rh and calcination at 350 °C) and reduction at 200 °C only a slight reduction in the specific surface area is observed over the TiO_2-ANP support. The rutile and brookite supports appear to retain most of their initial surface area during catalyst synthesis and the low temperature reduction. After the first reduction, the catalysts supported on the nanoparticle TiO_2 supports appear stable, as the specific surface areas of the Rh/TiO_2-ANP, Rh/TiO_2-RNP, and Rh/TiO_2-BNP catalysts are not significantly altered by reduction at 500 °C or the redox treatment (oxidation at 400 °C and a second reduction at 200 °C). In contrast, the Rh/TiO_2-RNR catalyst exhibits a 40% reduction in surface area after reduction at 500 °C. This is another indication that the rutile nanorods are less stable than the rutile nanoparticles and may undergo structural changes during reduction. It appears that the surface area is partially recovered during oxidation and the second reduction at 200 °C, which suggests that there is indeed restructuring of the TiO_2 nanorods. After this treatment, the specific surface area is 78% of the initial value. As expected, the specific surface area of the alumina support is higher than those of the TiO_2 supports, and is very stable during reduction, even at the higher reduction temperature (Table 2).

Table 2. Specific surface areas (SSAs) for Rh catalysts on TiO_2 and Al_2O_3 supports after various reduction-oxidation treatments.

Catalyst [a]	Support SSA [b] [m^2/g]	SSA after TPR-200 [c] [m^2/g]	SSA after TPR-500 [d] [m^2/g]	SSA after 2nd TPR-200 [e] [m^2/g]
Rh/TiO_2-ANP	45	34	32	37
Rh/TiO_2-RNP	27	27	28	29

Rh/TiO_2-BNP	29	28	29	29
Rh/TiO_2-RNR	53	50	30	39
Rh/γ-Al_2O_3	236	236	220	240

[a] Rh supported on commercial anatase TiO_2 nanoparticles (ANP), commercial rutile nanoparticles (RNP), a brookite nanoparticles (BNP), and rutile nanorods (RNR).
[b] BET surface area of the support.
[c] BET surface area of catalyst after reduction at 200 °C.
[d] BET surface area of catalyst after reduction at 500 °C.
[e] BET surface area of catalyst after reduction at 500 °C, oxidation at 400 °C and a second reduction at 200 °C.

3.5. CO Chemisorption

The amount of CO chemisorbed on the catalysts was also quantified to determine how the Rh metal surface area varied with the various redox treatments (Figure 4). In these experiments it is important to note that CO adsorption, even at room temperature, is known to disrupt small Rh nanoparticles on oxide supports [143, 144]. Therefore, no Rh dispersions are reported in this study, as the CO:Rh ratio will vary dependent on the catalyst treatments and the Rh particle size. However, CO chemisorption measurements are still useful as they, together with other catalysts characterization techniques, will provide information on how the catalysts are altered during the different treatments. Despite a slightly larger specific surface area of the anatase nanoparticles, the amount of CO chemisorbed on the Rh/TiO_2-RNP catalyst is higher. This is likely due to more favorable Rh-TiO_2 interactions between the ionic rhodium precursor and the rutile TiO_2 structure leading to a slightly higher Rh dispersion on the TiO_2-RNP support [145]. Higher metal dispersions on rutile compared with anatase TiO_2 have been observed on other TiO_2-supported metal catalysts as well [142, 146, 147]. However, higher dispersions are also reported on anatase TiO_2 [44], but this is typically due to a significantly higher surface area for the anatase support compared with the rutile TiO_2 support (larger differences than in this study). The CO uptake is also larger on the Rh/TiO_2-BNP compared with the Rh/TiO_2-ANP catalyst, despite the lower specific surface area of the TiO_2-BNP compared with the TiO_2-ANP support. This suggests stronger Rh-TiO_2 interactions with the brookite surface compared with the anatase structure, although the interactions may not be as strong as between the Rh and the rutile TiO_2 support. The largest CO uptake and therefore also initial Rh surface area is observed on the Rh/TiO_2-RNR catalyst, which could be due to the rutile TiO_2 phase together with the larger specific surface area compared with the other supports.

All catalysts exhibit a decrease in the CO uptake after reduction at 500 °C (Figure 4), which indicates that the accessible Rh metal surface area is smaller after this treatment on all TiO_2 supports. This could be due to sintering of the Rh metal particles or migration of TiO_x over the Rh metal particles. Another possibility is induction of electronic Rh-TiO_2 interactions that result in coordinative saturation of the Rh sites [48, 135, 148, 149].

Loss in Rh metal surface area due to sintering is typically permanent, while migration of TiO_x can be reversed by an oxidative treatment and a second reduction at a lower temperature (200 °C) [5, 6]. Less is known about the reversibility of electronic metal-support interactions. Figure 4 reveals that some of the original Rh metal surface area can indeed be recovered by the oxidation and re-reduction for the Rh/TiO_2-ANP, Rh/TiO_2-RNR, and Rh/TiO_2-BNP catalysts, while this treatment does not recover the original Rh metal surface area for the Rh/TiO_2-RNP catalyst. This suggests that the brookite TiO_2 behaves like anatase TiO_2 and results in reversible (or partially reversible) TiO_x migration over the Rh particles, while the rutile TiO_2 does not. The fact that the Rh/TiO_2-RNR catalyst exhibits a different behavior from the Rh supported on the rutile nanoparticles, is likely due to the presence of a brookite phase on this support. However, the fact that a brookite phase forms also indicates that the TiO_2 nanorods are not stable, despite the large fraction of the most stable (110) surface facets, and this may be why the rutile rods, but not the rutile nanoparticles, induce TiO_x migration. The incomplete recovery of CO chemisorption may result from some Rh particle aggregation or sintering during the high-temperature reductive treatment, although some TiO_x remaining on the Rh particles cannot be excluded [150].

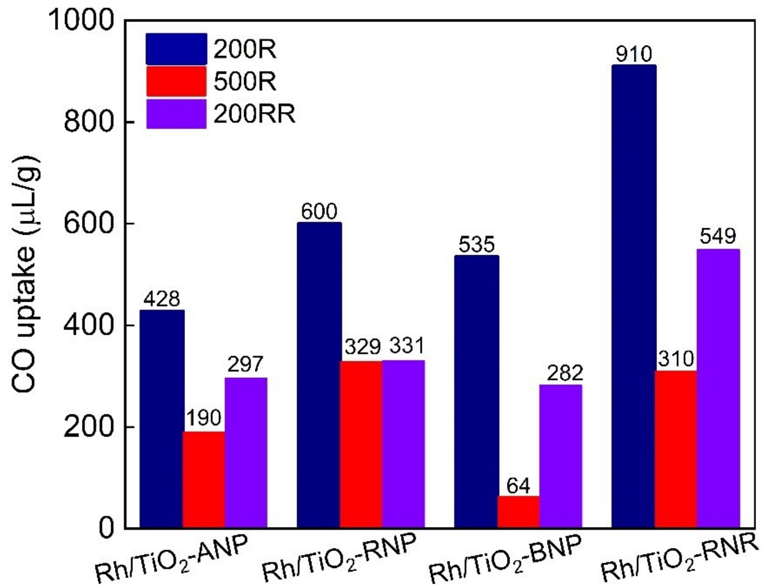

Figure 4. CO chemisorption for Rh/TiO_2-ANP, Rh/TiO_2-RNP, Rh/TiO_2-BNP, and Rh/TiO_2-RNR following TPR to 200 °C (200R), TPR to 500 °C (500R), and TPR to 500 °C followed by oxidation at 400 °C and re-reduction at 200 °C (200RR).

The CO uptake was also measured on the Rh/γ-Al_2O_3 (Table S2), but despite a 4-9 times larger surface area of the γ-Al_2O_3 support compared with the TiO_2 supports, very little CO is adsorbed on the Rh/γ-Al_2O_3 after the different reduction and oxidation treatments, see Table S2, and discussion in Supporting Information.

3.6. S/TEM Experiments

HR-TEM images were collected from all TiO_2-supported catalysts before and after reduction at 200 °C, 500 °C and after the redox treatment (reduction at 500 °C, oxidation at 400 °C followed by reduction at 200 °C). The TiO_2 nanoparticle sizes for the ANP and RNP supports are reasonably consistent with those reported from the manufacturer, and small Rh particles are evident in the higher resolution images of Figure 5(a-d). Consistent with the specific surface area measurements, the particle sizes of the BNP support are also in a similar range (Figure 5(e)). The HR-TEM images from the pure titania nanorods (TiO_2-RNR), before Rh deposition, reveal that the TiO_2 rods are between 10 and 40 nm in width with varying length (some up to 100 nm or more), as shown in Figure 5(g). The rods appear highly crystalline (Figure S3), and the surface facets are consistent with the most stable surface facet of the rutile structure, i.e., TiO_2 (110). As expected from the XRD measurements, no significant changes in the TiO_2 nanoparticles are observed for the different treatments of the ANP, RNP and BNP catalysts (Figure S4). The Rh nanoparticle sizes obtained from the HR-TEM images are all ~1.9 ± 0.6 nm, irrespective of reduction temperature (Figures S4-S5). Therefore, no significant sintering (particle growth) is observed on the Rh/TiO_2 catalysts, in contrast to what has been observed over Rh/CeO_2 catalysts [151]. The Rh (or RhO_y) nanoparticles are more difficult to observe on the BNP catalyst after reduction at 200 °C, but those that are visible do appear to be in this size range (Figure S4). It is evident from the HR-TEM data that the Rh particle size alone cannot explain the drastic differences in CO chemisorption observed over these catalysts [148, 152].

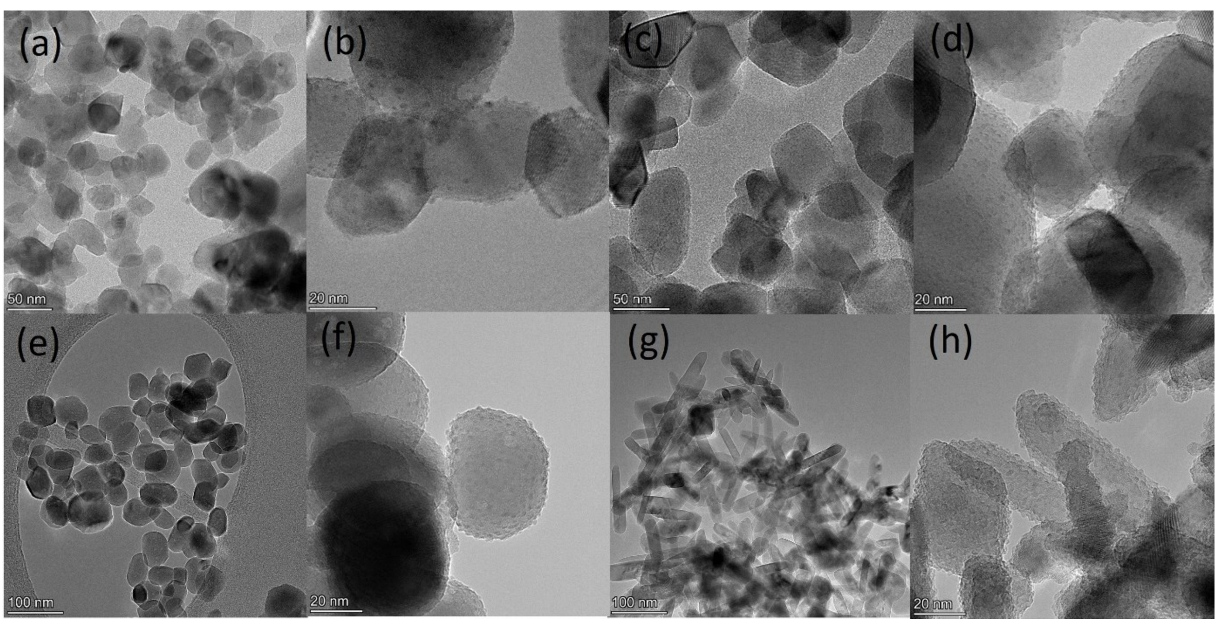

Figure 5. HR-TEM images obtained from: Rh/TiO_2-ANP after reduction at 200 ºC at two different magnifications (a) and (b), Rh/TiO_2-RNP after reduction at 200 ºC at two different magnifications (c) and (d), pure brookite nanoparticles (e) and Rh/TiO_2-BNP after 500 ºC reduction (f), pure TiO_2 nanorod (g), Rh/TiO_2-RNR after 200 ºC reduction (h). Scale bars are as follows: 50 nm: (a) and (c), 20 nm: (b), (d), (f) and (h), 100 nm: (e) and (g).

To further evaluate selected catalysts and confirm the structure of the TiO_2 supports, monochromated STEM-EELS mapping was performed to measure the relative contributions of anatase, rutile and brookite as described previously. The EEL spectra and phase mapping results obtained from the TiO_2 references are included in the Supporting Information (Figures S6 and S7, respectively). Consistent with previous reports [153-155], the data show that STEM-EELS can distinguish between the different phases of TiO_2 and confirm that the expected anatase, rutile and brookite phases are indeed the main structures observed in the ANP, RNP and BNP supports, respectively (Figure S7). In the case of the Rh/TiO_2-ANP catalyst after reduction at 500 ºC, STEM-EELS mapping (Figure 6(a) – (d)) shows that the main phase of TiO_2 is anatase, and the slight rutile impurity detected by XRD is evidently due to the presence of a few rutile nanoparticles. A minor contribution from brookite also appears to be present, but not with sufficient long-range ordering such that it would be detectable with XRD or Raman.

In contrast to the nanoparticle TiO_2 supports (ANP, RNP and BNP), where the TEM images of the support are not visibly altered, significant changes are observed for the catalysts supported on the rutile TiO_2 nanorods (RNR) after the different reduction treatments. After Rh deposition (catalyst synthesis followed by reduction at 200 ºC), there are some changes observed in the TiO_2 nanorod support, as may have been expected due to the introduction of a brookite phase. The majority of the Rh/TiO_2-RNR catalyst after reduction at 200 °C still consists of TiO_2 nanorods, but the width is increased in some cases, and some TiO_2 nanoparticles are visible (Figure S3). Small Rh nanoparticles are visible on the TiO_2 nanorods and TiO_2 nanoparticles at the higher magnification (Figure 5(h) and S4) and their average particle size is slightly smaller (~1.4 ± 0.3 nm) compared with the Rh particles on the TiO_2-ANP and TiO_2-RNP supports (1.7-1.8 ± 0.6 nm after the first 200 °C reduction, Figure S5). This is consistent with the CO chemisorption measurements, i.e., a higher CO uptake over the Rh/TiO_2-RNR catalyst, suggesting a larger Rh surface area and smaller Rh particles on the TiO_2-RNR support. After reduction at 500 ºC significant restructuring of the TiO_2 nanorods is observed. In fact, very few rods are observed and large amounts of TiO_2 nanoparticles are visible after this treatment (Figure S3). Since no significant increase in brookite phase is observed in the XRD patterns obtained from this catalyst after reduction at 200 versus 500 °C, monochromated STEM-EELS mapping was used to measure of the relative contributions of anatase, rutile and brookite in this catalyst; it should be noted that while anatase was not observed via XRD or Raman spectroscopy, it was still included as a possible phase for STEM-EELS phase mapping [108]. Figure 6 reveals that the contribution from brookite is larger than expected even after reduction at 200 °C. The nanoparticles that have formed appear to consist mainly of brookite, while most rods consist of the rutile phase. In addition, there is also a contribution from anatase TiO_2, and this contribution is very inhomogeneous across the sample (compare Figures 6 and S8). According to the STEM-EELS mapping, the rutile phase makes up 53% of the sample, while the contributions from anatase and brookite are 23% and 24%, respectively. Other areas have almost equal contributions from the three phases (Figure S8). Even with the significant restructuring of the support, only a slight increase in the Rh particle size to 1.9 ± 0.4 nm is discerned (Figures S4-S5). While this is a slightly larger increase than that observed over the Rh/TiO_2-ANP and Rh/TiO_2-RNP catalysts, none of the observed increases in Rh particle size is statistically significant (Figure S5).

HAADF-STEM Image Anatase rutile brookite

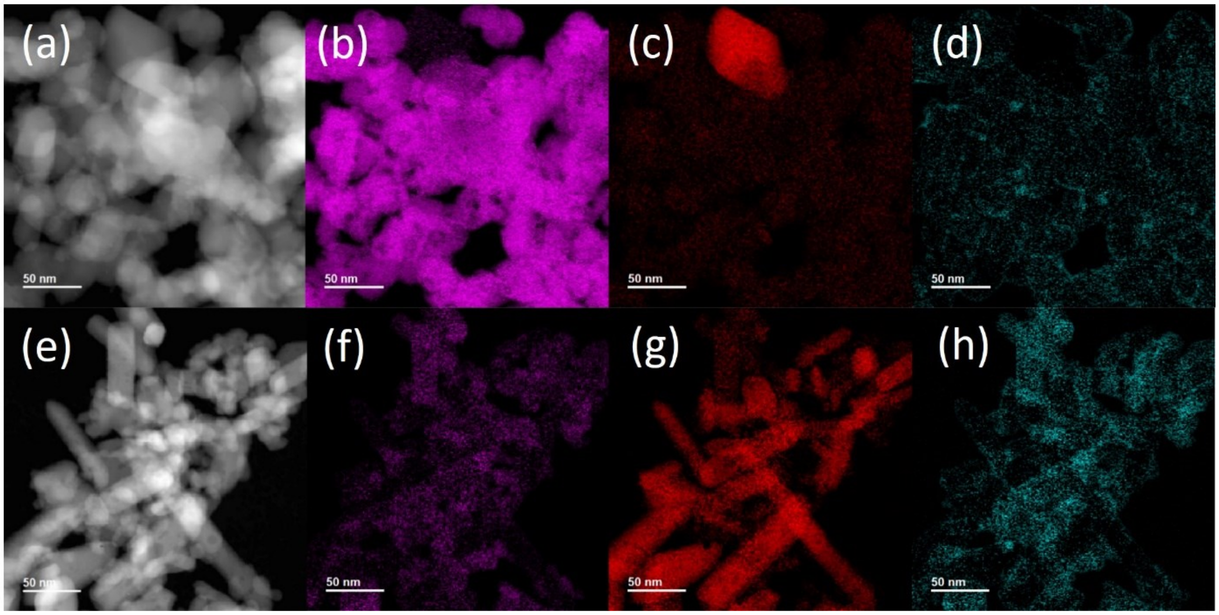

Figure 6. Monochromated STEM-EELS phase mapping for the Rh/TiO_2-ANP catalyst after reduction at 500 °C (top row) and the Rh/TiO_2-RNR after reduction at 200 °C (bottom row). (a) and (e) HAADF-STEM images of the analysis areas, (b) and (f) anatase contributions, (c) and (g) rutile contributions, (d) and (h) brookite contributions. The contrast limits for the phase maps for each analysis area were set equally to allow the contributions of each phase to be accurately reflected.

3.7. Hydrogenation of Propylene

To determine the influence of the different reduction treatments on catalytic activity, propylene hydrogenation was selected as the probe reaction. As mentioned, this reaction was selected since hydrogenations are facile over Rh catalysts, which translates to low reaction temperatures, a requirement for avoiding SMSIs under the reducing reaction conditions. In fact, hydrogenation of ethylene is so facile over Rh/TiO_2 catalysts that it is not possible to obtain a typical light-off curve over these catalysts without cooling the catalyst below room temperature [51], and, as a result, the difference in ethylene hydrogenation activity between Rh on anatase and rutile TiO_2 supports is small (Figure S9). It should also be noted that Rh on Al_2O_3, a non-reducible support, exhibits a very different behavior compared with Rh on anatase and rutile TiO_2 (see Figure S9 and discussion in Supporting Information). To evaluate structure-dependent differences in activity for the Rh/TiO_2 catalysts, propylene was selected as the reactant as this is a commonly used probe reaction [95-100]. In addition, low concentrations (2% propylene) with dilute catalyst were used to avoid hot spots in the reactor. The reaction was run under stoichiometric conditions, i.e., with a propylene-to-hydrogen ratio of 1:1, after different redox treatments to evaluate structure-dependent SMSI effects.

3.7.1. Rhodium on Anatase Titania Nanoparticles. The Rh/TiO_2-ANP catalyst is highly active after reduction at 200 °C and close to 90 % of the propylene is converted at a temperature of 42 ± 5 °C (Figure 7). This is in line with literature data over supported metal catalysts [93], but direct comparisons are difficult due to differences in active metal loadings and reaction conditions, such as propylene-to-hydrogen ratios. The maximum conversion observed over this catalyst is 91% at 80 °C under the reaction conditions used in this study. After reduction at 500 °C the catalytic activity is significantly reduced, as expected from the lower CO uptake (and thus lower accessible Rh metal surface area) after this treatment. Consistent with the CO chemisorption measurements, i.e., recovery of the Rh sites, the catalytic activity can be regenerated over the Rh/TiO_2-ANP after a 400 °C oxidation and re-reduction at 200 °C. This again suggests that the losses in CO uptake and hydrogenation activity after reduction at 500 °C are indeed due to blocked active sites from migration of TiO_x over the metal sites, which is reversed by the 400 °C oxidation treatment.

The activity over the Rh/TiO_2-RNP catalyst after reduction at 200 °C is significantly lower than over the catalyst supported on the anatase TiO_2 nanoparticles. Under the conditions in this study, the maximum propylene conversion over this catalyst is only 64% at 80 °C. The CO uptake measurements reveal that this is not likely due to differences in the Rh surface area between the TiO_2-ANP and TiO_2-RNP catalysts (since the CO uptake is higher on the Rh/TiO_2-RNP catalyst) and suggests that the TiO_2 structure does influence the supported Rh and therefore also the propylene hydrogenation activity over these catalysts. This is in stark contrast to the ethylene hydrogenation activity over these catalysts at a H_2:C_2H_4 ratio of 2:1 (Figure S9), where both the Rh/TiO_2-ANP and Rh/TiO_2-RNP catalysts converted close to 100% of the ethylene at 40 °C. This stresses the importance of carefully selecting the probe reaction and reaction conditions when studying the effect of support structure on catalytic activities.

The Rh/TiO_2-RNP catalyst also exhibits a distinct loss in propylene hydrogenation activity after reduction at 500 °C, although the loss is smaller than for the Rh/TiO_2-ANP catalyst. However, in the case of the Rh/TiO_2-RNP catalyst the activity cannot be recovered by a 400 °C oxidation and re-oxidation at 200 °C. This permanent deactivation after reduction at 500 °C is consistent with the permanent loss in CO uptake (Figure 4 and 7) indicating that irreversible changes to the Rh/TiO_2-RNP catalyst have occurred during the high temperature reduction.

The activity of the Rh on the brookite TiO_2 nanoparticles in the hydrogenation of propylene is similar to the Rh supported on rutile TiO_2 supports, despite the higher CO uptake observed on the Rh/TiO_2-RNP catalyst. The maximum propylene conversion observed is 65% between 60 ºC and 80 °C. While this could indicate more active Rh species on the brookite TiO_2 support, it is also possible that the mobility of rhodium carbonyls is higher on the rutile TiO_2 supports (which would lead to a larger CO uptake). These results suggest that the Rh on the anatase TiO_2 nanoparticles is more active compared with Rh on either brookite or rutile TiO_2 supports. As expected, the 500 °C reduction treatment results in a loss of propylene hydrogenation activity, but the loss in activity is not as pronounced as may have been expected from the loss in CO uptake over this catalyst after reduction at 500 °C. The propylene hydrogenation activity can be recovered by a redox treatment, indicating that the high-temperature reduction did induce TiO_x migration over the Rh metal particles also on the brookite TiO_2 support. Therefore, these results suggest that anatase and brookite are prone to TiO_x migration, while rutile is not. Also, the large difference in CO uptake between reduction at 200 versus 500 °C, is likely due to more mobile rhodium carbonyls on the catalyst reduced at 200 °C compared with reduction at 500 °C where the TiO_x overlayer inhibits some of the rhodium carbonyl mobility.

Despite having the largest CO uptake, the propylene hydrogenation activity is the lowest over the Rh/TiO_2-RNR catalyst. Since the TEM images indicate that the Rh particle size is smaller on this support compared with the TiO_2-ANP and TiO_2-RNP supports, this suggests that the Rh on this surface is the least active amongst the TiO_2-supported catalysts. As expected, based on the results from the other TiO_2-supported catalysts, a distinct loss in activity is observed after reduction at 500 °C. However, despite the high rutile content of this catalyst, the activity can be regenerated by the redox treatment (oxidation at 400 °C and re-reduction at 200 °C). This again suggests that the behavior of this catalyst with redox treatment is dominated by the brookite (or anatase) phase(s) present after catalyst synthesis and reduction treatment, although it is not possible to rule out TiO_x migration caused by the lower stability of the rutile TiO_2 phase of the nanorods under reducing conditions.

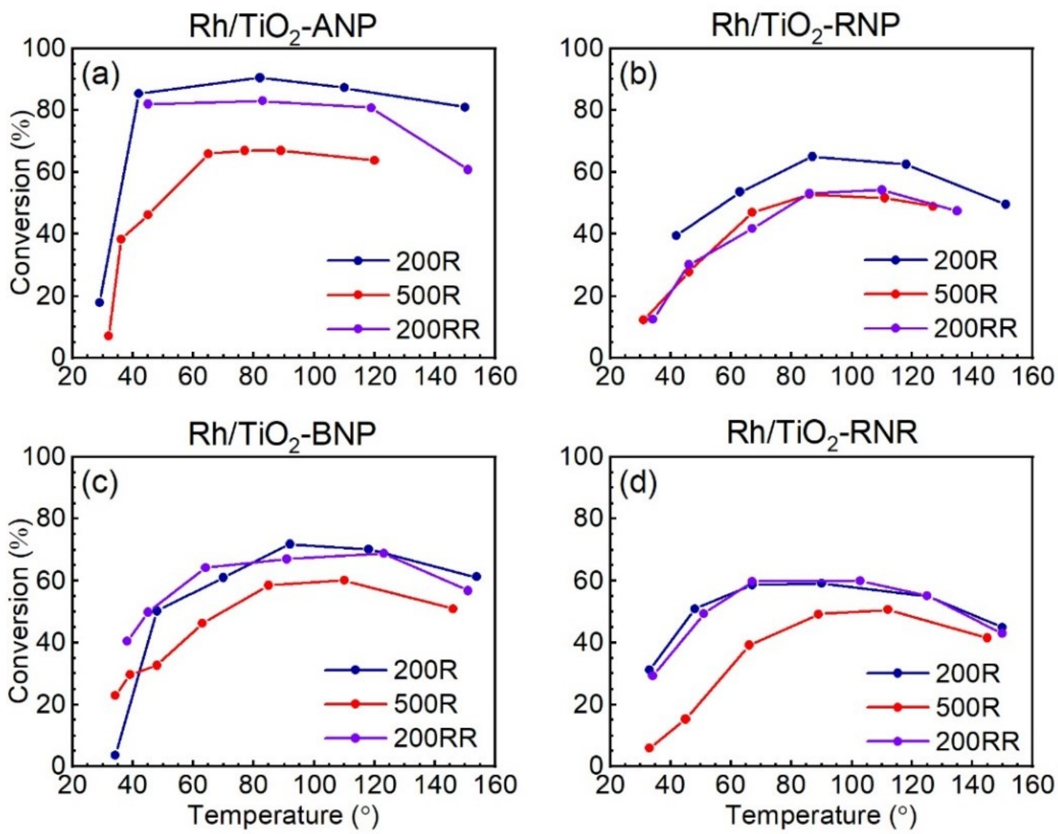

Figure 7. Temperature dependence of propylene conversion during hydrogenation to propane over (a) Rh/TiO_2-ANP, (b) Rh/TiO_2-RNP, (c) Rh/TiO_2-BNP, and (d) Rh/TiO_2-RNR following TPR to 200 °C (200R), TPR to 500 °C (500R), and TPR to 500 °C followed by oxidation at 400 °C and re-reduction at 200 °C (200RR). Reaction conditions: 10 mg of catalyst diluted with 20 mg γ-Al_2O_3 with C_3H_6: 2 sccm, H_2: 2 sccm, N_2: 3 sccm, He: 91 sccm flow rate.

Since the anatase and brookite phases of TiO_2 are metastable, the performance with time on stream was also evaluated for these catalysts. The catalysts were evaluated at 80 °C, which is close to the temperature at which the maximum conversion is observed for all catalysts. As can be seen in Figure 8(a), the Rh/TiO_2-ANP catalyst is surprisingly stable with time on stream considering the metastable anatase phase of TiO_2. This catalyst maintains a propene conversion of 90% during the eight hours of the experiment. The Rh/TiO_2-RNP catalyst is also stable with time on stream, but at a lower propene conversion. In contrast, the Rh/TiO_2-BNP catalyst exhibits a slight decline in activity as a function of time. After eight hours under reaction conditions, the catalyst has lost 7% of the initial activity. The largest loss in activity (20%) is observed over the Rh/TiO_2-RNR catalyst, which is expected considering the structural changes observed during the reduction treatments.

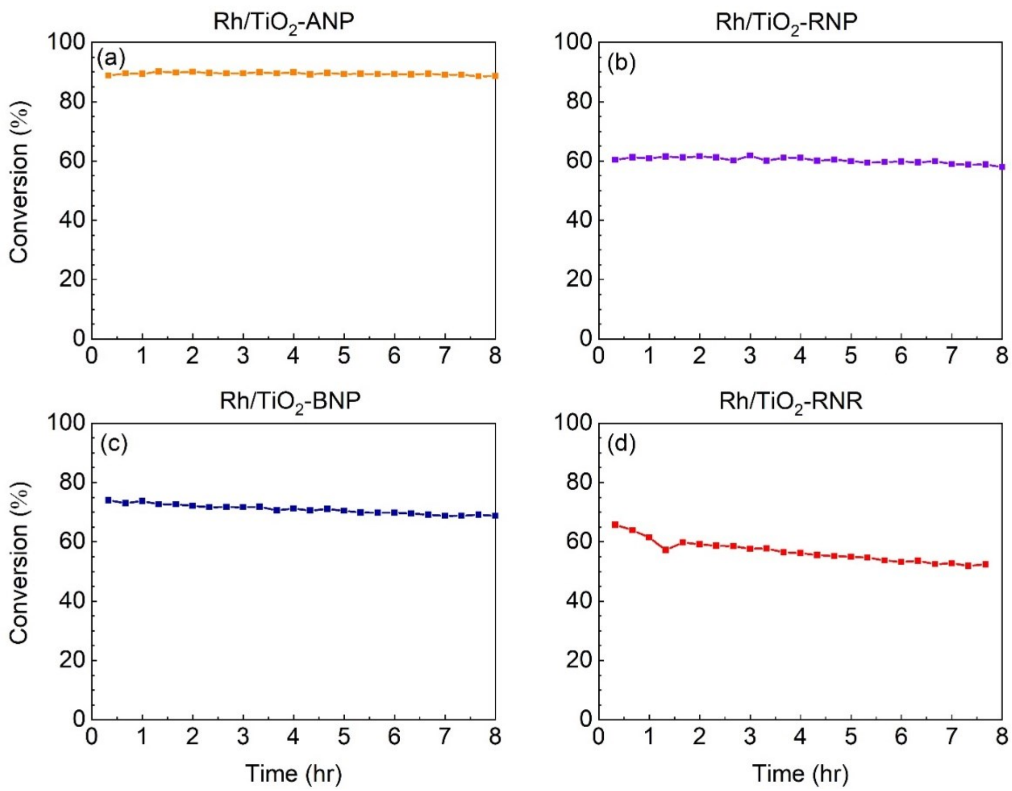

Figure 8. Propylene conversion during hydrogenation to propane as a function of time over (a) Rh/TiO_2-ANP, (b) Rh/TiO_2-RNP, (c) Rh/TiO_2-BNP, and (d) Rh/TiO_2-RNR after a reductive pretreatment at 200 °C. Reaction conditions: 10 mg of catalyst diluted with 20 mg γ-Al_2O_3 with C_3H_6: 2 sccm, H_2: 2 sccm, N_2: 3 sccm, He: 91 sccm flow rate.

Since a small rutile phase was observed in the TiO_2-ANP support, two additional catalysts were prepared with anatase TiO_2 supports having a smaller average particle size compared with the TiO_2-ANP support (15 nm). TiO_2 particles with average particle sizes of 10 nm and below have larger specific surface areas than the TiO_2-ANP support, but more stable anatase phases. As expected, no XRD peaks or Raman features due to rutile TiO_2 can be detected in the TiO_2-ANP10 and TiO_2-ANP05 supports (average particle sizes of 10 and 5 nm respectively) and catalysts before or after reduction treatments (Figure S10). The reaction results from the Rh/TiO_2-ANP10 and Rh/TiO_2-ANP05 catalysts reveal that the smaller TiO_2 particles yield inferior catalytic activities compared with the Rh/TiO_2-ANP catalyst (Figure S11) despite slightly higher CO uptakes over the Rh/TiO_2-ANP10 and Rh/TiO_2-ANP05 catalysts (Table S2). The reason for this unexpected result will be discussed below.

3.8. X-Ray Photoelectron Spectroscopy

To further evaluate differences in the electronic structure of rhodium, *ex situ* XPS data were collected on the Rh/TiO_2-ANP, Rh/TiO_2-RNP and Rh/TiO_2-BNP catalysts after the different redox treatments. While *in situ* treatments are preferred, *ex situ* reductions can provide information on supported metal catalysts, if the air exposure after reduction is limited and occurs only at room temperature. The XPS binding energies were adjusted slightly to align the C 1s peaks at 284.6 eV as shown in Figure 9(a). The signal intensities from all Rh 3d peaks are low (Figures 9(b) and S12), due to the low Rh concentrations (0.4% by weight or 0.3 mol% of Rh on TiO_2). Due to the low signal-to-noise, peak fittings were not attempted for the Rh 3d peaks, and even for the O 1s and Ti 2p peaks, peak fittings are not trivial (see Figures S13 and S14 and description in Supporting Information for more details). The discussions are therefore focused mainly on qualitative rather than quantitative differences between the catalysts.

3.8.1. Rhodium on Anatase Titania Nanoparticles. The center of the Rh $3d_{5/2}$ peak obtained from the Rh/TiO_2-ANP catalyst after reduction at 200 °C is located at 307.5 eV (Figure 9(b)), which is a slightly higher than the binding energy reported for Rh metal (307.1 eV) [156, 157], but lower than the binding energy of Rh_2O_3 (309.1 eV) [158]. The peak is also broad, suggesting that multiple species with oxidation states between Rh^0 and Rh^{3+} are present on the surface of this catalyst. This could be due to a thin oxide layer (RhO_y, with $y \leq 1.5$) from the air exposure following the reduction (during transfer to the XPS instrument) and it is expected that the relative contribution from Rh^{3+} from an air exposure is higher on small Rh particles compared with larger Rh particle sizes. It is also possible that strong interactions between the rhodium ions and the TiO_2 support result in difficult to reduce $Rh^{\delta+}$ species, so the reduction of Rh_2O_3 to Rh metal is incomplete during reduction at 200 °C. In addition, the formation of rhodium hydroxides during the low-temperature reduction cannot be excluded. The presence of hydroxyl groups on the surface of this catalyst is evident as a distinct shoulder at 531.5 eV on the main O 1s peak which is due to the lattice oxygens in TiO_2 (at 529.4 eV, Figure 9(c)) [156]. However, it is not possible to determine from the O 1s peak if the hydroxyl groups are associated with rhodium or titanium. Due to the size of the shoulder, it is expected that at least some of these hydroxyl groups are due to the TiO_2 support. In fact, two O 1s peaks at 531.0 and 532.2 eV are needed to fit this part of the O 1s region well (Figure S14). The peak positions are indicative of hydroxyl groups, perhaps two different types of hydroxyl groups or adsorbed water-like species [159]. The Ti $2p_{3/2}$ peak is located at 458.5 eV, consistent with the binding energy expected for Ti^{4+} in TiO_2 (Figure 9(d)) [160]. The full width at half maximum (FWHM) of the Ti $2p_{3/2}$ peak is narrow, 1.16 eV, slightly broader than the FWHM reported for TiO_2 (0.99 eV) [160], suggesting the presence of additional TiO_x (or $TiO_z(OH)_w$) species. The Ti 2p region is difficult to fit with only three peaks, suggesting the presence of multiple species, such as TiO_x with $x < 2$, or $TiO_z(OH)_w$) species (with $z < 2$ and $1 \leq w \leq 4$) [157, 161]. The O:Ti ratio is very large (> 4), much larger than the expected 2:1 from TiO_2, which would be consistent with the presence of hydroxylated Ti^{3+} or Ti^{4+} species, such as $Ti(OH)_3$, $TiO(OH)_2$ or $Ti(OH)_4$ and contributions from Rh-related oxygen species (see Table 3 for the surface composition on a carbon-free basis). As expected, the surface is enriched in Rh (1.6 atom%) compared to the bulk Rh content (0.3 mol% of Rh on TiO_2 is equal to 0.1 atom% of Rh on a Rh, Ti and O atomic basis).

Reduction at 500 °C shifts the Rh 3d peaks to slightly lower binding energies, indicating an increase in the Rh^0 content, i.e. more of the Rh_2O_3 on the fresh catalyst is reduced to Rh metal at 500 °C compared with reduction at 200 °C (Figure 9(b)). However, a significant shoulder at higher binding energies (relative to the Rh^0 peak at 307.1 eV) reveals that some $Rh^{\delta+}$ species remains in the near surface region. A reduction in the 532-eV shoulder on the O 1s peak is consistent with the removal of some hydroxyl groups (Figure S14). A decrease in the Ti 2p peak at 457.9 eV is also observed (Figure S13 and Table S3). A feature at 528 eV is needed to fit the O 1s region well, and this feature could be due to oxygen species at the Rh-TiO_x interface. This would explain the presence of Ti species with lower-than-expected binding energies (Figure S13). However, due to the low Rh content in these catalysts the uncertainties in these peaks (and the peak fittings) are high. The atomic O:Ti ratio is not altered significantly by the high temperature reduction (Table 3), suggesting that the surface hydroxyl groups are associated with $TiO(OH)_2$ or $Ti(OH)_z$ and are not removed by the high temperature reduction. Consistent with geometric SMSIs, i.e. a TiO_x layer over the Rh particles, the Rh:Ti ratio is smaller after the high temperature reduction, although the change in Rh concentration from 1.6% to 0.9% is small and the uncertainty of these numbers is high.

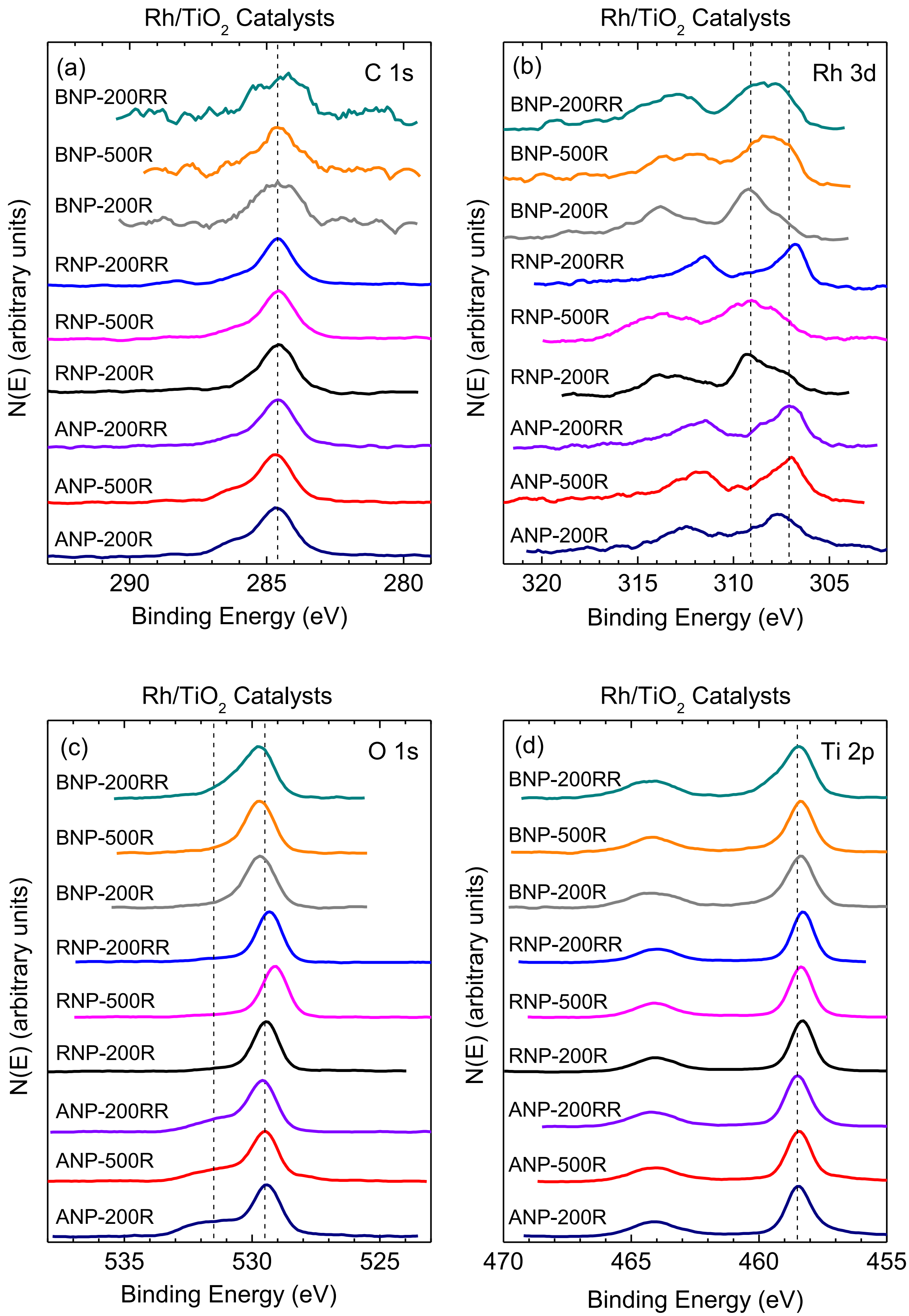
Rh/TiO$_2$ Catalysts
(a)
C 1s
BNP-200RR
BNP-500R
BNP-200R
RNP-200RR
RNP-500R
RNP-200R
ANP-200RR
ANP-500R
ANP-200R
N(E) (arbitrary units)
290
285
280
Binding Energy (eV)
Rh/TiO$_2$ Catalysts
(b)
Rh 3d
BNP-200RR
BNP-500R
BNP-200R
RNP-200RR
RNP-500R
RNP-200R
ANP-200RR
ANP-500R
ANP-200R
N(E) (arbitrary units)
320
315
310
305
Binding Energy (eV)
Rh/TiO$_2$ Catalysts
(c)
O 1s
BNP-200RR
BNP-500R
BNP-200R
RNP-200RR
RNP-500R
RNP-200R
ANP-200RR
ANP-500R
ANP-200R
N(E) (arbitrary units)
535
530
525
Binding Energy (eV)
Rh/TiO$_2$ Catalysts
(d)
Ti 2p
BNP-200RR
BNP-500R
BNP-200R
RNP-200RR
RNP-500R
RNP-200R
ANP-200RR
ANP-500R
ANP-200R
N(E) (arbitrary units)
470
465
460
455
Binding Energy (eV)

Figure 9. XPS data, (a) C 1s, (b) Rh 3d, (c) O 1s, and (d) Ti 2p, collected from Rh/TiO_2-ANP (ANP), Rh/TiO_2-RNP (RNP), and Rh/TiO_2-BNP (BNP) after the following redox treatments; TPR to 200 °C (200R), TPR to 500 °C (500R), and TPR up to 500 °C followed by oxidation at 400 °C and re-reduction at 200 °C (200RR).

After a redox treatment following the 500 °C reduction (oxidation at 400 °C and re-reduction at 200 °C) the Rh 3d peaks are similar to the peaks obtained after the 500 °C reduction (Figure 9(b)). Any differences in the Rh 3d peaks cannot be distinguished from the signal-to-noise (Figure S12). The Rh concentration and the Rh:Ti ratio are slightly higher after this treatment, consistent with reversal of TiO_x migration over Rh, but the low signal-to-noise (due to the low Rh content) results in uncertain Rh:Ti ratios. Furthermore, a TiO_x coating only a few atomic layers thick over the small Rh particles (< 2 nm) supported on TiO_2 nanoparticles (on the order of 15-50 nm) makes this even more challenging due to the probing depth of XPS (several atomic layers beyond the surface) and the powder samples add to the challenge (compared with thin films). Identification of a TiO_x overlayer with XPS has been done previously, but on catalysts with higher Rh loadings on the TiO_2 support or on model catalysts where Rh has been deposited on TiO_2 (110) thin films [74, 82, 83]. In our samples, the Rh content is very low and any increase in the Rh:Ti ratio due to the removal of the TiO_x overlayer is difficult to observe as it can be outweighed by a slight increase in Rh particle size (the latter would result in a decrease in the Rh:Ti ratio).

Table 3. Elemental compositions and ratios for Rh catalysts supported on anatase and rutile TiO_2 after various reduction-oxidation treatments.

Element or Ratio	Catalyst [a]								
	ANP			RNP			BNP		
	200R	500R	200RR	200R	500R	200RR	200R	500R	200RR
Rh	1.6%	0.9%	1.4%	1.2%	1.5%	1.1%	1.6%	0.6%	1.1%
Ti	17%	18%	22%	27%	25%	31%	27%	26%	30%
O	81%	81%	76%	72%	68%	72%	68%	74%	69%
Rh/Ti Ratio	0.09	0.05	0.06	0.05	0.05	0.04	0.05	0.02	0.04
O/Ti Ratio	4.7	4.6	3.4	2.7	2.2	2.7	2.2	2.9	2.3

[a] Elemental composition [Atom %] determined from the XPS data. Rh supported on commercial anatase TiO_2 nanoparticles (ANP) and commercial rutile TiO_2 nanoparticles (RNP) reduced at 200 °C (200R), 500 °C (500R) and reduced a second time at 200 °C after reduction at 500 °C and oxidation at 400 °C (200RR).

3.8.2. Rhodium on Rutile Titania Nanoparticles. The Rh $3d_{5/2}$ peak obtained from the Rh/TiO_2-RNP catalyst after reduction at 200 °C has a significantly higher contribution from rhodium oxide (binding energies around 309 eV) compared with the Rh/TiO_2-ANP catalyst. This is consistent with literature stating that Rh_2O_3 is more difficult to reduce when supported on rutile TiO_2 compared with anatase TiO_2 [73]. It is also consistent with the lower hydrogen uptake during the TPR measurements. This could be due to the stronger electronic interactions between $Rh^{\delta+}$ and rutile TiO_2 compared with anatase TiO_2, i.e. stronger interactions that resulted in a higher dispersion of Rh on rutile compared with anatase TiO_2 supports and a slower hydrogen uptake during TPR. Interestingly, the number of hydroxyl groups appears to be significantly smaller on the Rh/TiO_2-RNP compared with the Rh/TiO_2-ANP catalyst. Two O 1s peaks are still needed to fit the O 1s region, but with considerably reduced peak intensities and the peak positions are at slightly lower binding energies 530.5 and 531.7 eV (Figure S14). The O:Ti ratio is still larger than the 2:1 expected from TiO_2, but it is significantly lower than on the Rh/TiO_2-ANP catalyst (Table 3). The O:Ti ratio larger than two is in this case partly due to the fact that some oxygen is associated with the rhodium on the surface. The Ti $2p_{3/2}$ peak fitting yields a slightly lower binding energy (458.3 eV, Table S3) compared with the Ti $2p_{3/2}$ peak obtained from Rh/TiO_2-ANP (458.4-458.5 eV). This is consistent with reported binding energy differences between the Ti $2p_{3/2}$ peaks of rutile and anatase TiO_2 [159]. Only three Ti $2p_{3/2}$ are needed to fit the Ti 2p region, and the contribution from the state at low binding energy (457.3 eV) is smaller on the rutile TiO_2 compared with the anatase TiO_2 support. This is consistent with the lower O:Ti ratio, and thus a smaller contribution from hydroxylated Ti^{3+} on the rutile TiO_2. This trend is the same for all Rh/TiO_2-RNP catalysts, i.e. a smaller concentration of hydroxyl groups in the O 1s region and a lower Ti^{3+} content (peak at 457.3 eV), as evident in Figures 9, S13, S14 and Table S3. These observations, the lower contribution from hydroxyl groups to the O 1s peak, the lower O:Ti ratio, and the higher contribution from $Rh^{\delta+}$ species on the Rh/TiO_2-RNP catalyst further supports that the hydroxyl groups on the surface of the Rh/TiO_2-ANP catalyst are associated with the TiO_2 supports ($TiO_z(OH)_w$). The Rh surface concentration and the Rh:Ti ratio are slightly smaller on the Rh/TiO_2-RNP compared with the Rh/TiO_2-ANP catalyst, but the uncertainties in the numbers are high due to the low Rh content.

Even reduction at 500 °C does not appear to reduce more of the Rh_2O_3 on the surface of the RNP support. In fact, it looks like the center of the Rh 3d peaks have shifted to higher binding energies, suggesting the presence of a more electron-deficient $Rh^{\delta+}$ surface species compared with the catalyst reduced at 200 °C, even though the oxygen concentration is lower on the catalyst surface after the high-temperature reduction. This may seem counterintuitive but could mean that there is some rearrangement occurring during the high temperature reduction. Only a slight decrease in the Ti $2p_{3/2}$ peak at 459.2 eV (likely due to hydroxylated Ti^{4+} species) is observed, and this decrease is consistent with the lower O:Ti ratio. The O 1s peak appears to be shifted to lower binding energies (529.1 eV), and this has been observed in TiO_2 samples exposed to water [161]. It appears that the Rh concentration is slightly higher after the high-temperature reduction, but this is mainly due to the lower oxygen concentration (Table 3). No observable change in the Rh:Ti ratio can be detected between reduction at 200 °C and 500 °C. The decrease in CO chemisorption is therefore likely due to the higher concentration of electron-deficient $Rh^{\delta+}$ surface species, which are more coordinatively saturated than the original species. The results are consistent with strong electronic interactions between Rh and the rutile TiO_2 support, and reveal very different behaviors between the anatase and rutile TiO_2 supports during reduction at 500 °C.

After oxidation and re-reduction at 200 °C, the Rh 3d peaks have been altered. Most of the Rh is now present as Rh metal, and, while it may look like the Rh 3d peak has shifted to lower binding energies (306.8 eV), the apparent shift is due to the presence of more Rh^0 compared with the Rh/TiO_2-ANP catalyst (See Figure S12). Rearrangement of Rh particles during redox treatments has been observed previously [131]. The O 1s peak has shifted back to its original position (within the error bars of the measurements), but with a slightly higher contribution from the state at 531.7 eV (Table S3). Changes in the Ti 2p peaks with the redox treatment are insignificant (Figure S14 and Table S3). It is surprising that the hydrogenation activity is not improved on this catalyst, but points to the fact that the oxidation state of rhodium is only one parameter that influences the activity.

3.8.3. Rhodium on Brookite Titania Nanoparticles. The carbon content on the Rh/TiO_2-BNP catalysts is significantly lower compared with the catalysts supported on TiO_2-ANP and TiO_2-RNP, which makes charge shift adjustments more challenging. However, due to the neutralization mode on the XPS instrument, very little adjustment is needed. After reduction at 200 °C, most of the rhodium on the surface of the brookite TiO_2 is still in an oxidized state. The Rh 3d peaks are similar to those obtained from the Rh/TiO_2-RNP catalyst, suggesting strong interactions also between Rh and brookite TiO_2. The $Rh^{\delta+}$:Rh^0 ratio appears to be slightly higher on the BNP compared with the RNP support (Figure 9(b)). The large contribution from oxidized rhodium species on the brookite nanoparticles is surprising considering the high hydrogen uptake measured using TPR over this catalyst compared with the Rh/TiO_2-ANP and Rh/TiO_2-RNP catalysts (Figure 3 and Table S1). However, it is a further indication that significant hydrogen spillover occurs on the brookite support even at a reduction temperature as low as 200 ºC. The high oxidation state of the rhodium is also surprising considering the high CO uptake compared with the Rh/TiO_2-ANP catalyst, since oxygen is expected to block CO uptake. This could indicate that the strong metal support interactions lead to Rh metal particles which are easily oxidized during air exposure at room temperature, i.e., during transport to the XPS instrument. The O 1s peak obtained from the Rh/TiO_2-BNP catalyst is broader than the one obtained from the Rh/TiO_2-RNP catalyst (Table S3), but the contribution from hydroxyl groups is smaller than on the Rh/TiO_2-ANP catalyst (Figure S14). A significant shoulder at higher binding energies (459.1 eV) is observed in the Ti 2p peaks obtained from the Rh/TiO_2-BNP catalyst, suggesting the presence of electron-deficient Ti^{4+} species, likely hydroxylated titania, such as $TiO(OH)_2$. Since the O:Ti ratio (2.2) is similar to that obtained from the Rh/TiO_2-RNP catalyst it is unlikely that the hydroxyl species originate from $Ti(OH)_4$.

Reduction at 500 ºC increases the contribution from the metallic Rh. Compared with the other catalysts the $Rh^{\delta+}$:Rh^0 ratio on the Rh/TiO_2-BNP catalyst after this reduction treatment is lower compared with the Rh/TiO_2-RNP catalyst, but higher than on the Rh/TiO_2-ANP catalyst. It is interesting to note that the high-temperature reduction increases oxygen concentration on the surface of the Rh/TiO_2-BNP catalyst. This is in contrast to the Rh/TiO_2-RNP catalyst, where the oxygen content was decreased after reduction at 500 °C. Despite the increase in the O:Ti ratio after reduction at 500 ºC, no detectable changes are observed in the O 1s peaks, and the Ti 2p peaks are also similar between reduction at 200 and 500 ºC. The O 1s binding energy on the Rh/TiO_2-BNP catalyst is higher (529.7 eV) compared with the Rh/TiO_2-RNP and Rh/TiO_2-ANP catalysts (529.4 eV), but the contribution from hydroxyl groups to the O 1s peak (species with binding energies above 530.5 eV) is still lower than on the Rh/TiO_2-ANP catalyst after the same treatment. The Rh concentration and the Rh:Ti ratio are lower after reduction at 500 ºC, which is consistent with Ti migrating over Rh. This behavior is similar to that of the Rh/TiO_2-ANP catalyst, but it is evident that the Rh species are different on the TiO_2-ANP and TiO_2-BNP supports, which can explain the differences in activity between these catalysts.

After the extended redox treatment (reduction at 500 °C, oxidation at 400 °C and re-reduction at 200 °C), distinct differences between the Rh/TiO_2-BNP and the Rh/TiO_2-ANP and Rh/TiO_2-RNP catalysts are observed in the XPS data. The contribution from oxidized rhodium is still significant on the Rh/TiO_2-BNP catalyst after this redox treatment. Furthermore, both the O 1s and Ti 2p peaks are significantly broader with increased contributions from states at higher binding energies in the XP spectra obtained from the Rh/TiO_2-BNP catalyst (four peaks are needed to fit the Ti 2p region well). It appears that multiple O-containing Rh and Ti species are present on the surface of the Rh/TiO_2-BNP catalyst after this treatment. The Rh concentration and Rh:Ti ratio have increased slightly, consistent with reversal of TiO_x migration over the Rh particles.

3.8.4. Rhodium on Additional Anatase Titania Nanoparticles. Since the Rh/TiO_2-ANP10 and Rh/TiO_2-ANP05 catalysts exhibited unexpectedly low activity in the hydrogenation of propene, they were also subjected to XPS measurements. As for the Rh/TiO_2-RNP and Rh/TiO_2-BNP catalysts, most of the rhodium on the surface of the TiO_2-ANP10 and TiO_2-ANP05 supports is in an oxidized state after reduction at 200 °C (Figure S15). This is unexpected, as the TPR measurements reveal Rh_2O_3 reduction temperatures closer to those of the Rh/TiO_2-RNP and Rh/TiO_2-BNP catalysts (Figures 3 and S2), i.e. lower than the Rh_2O_3 reduction temperature on the TiO_2-ANP (15 nm) support. This may indicate that the surface of the Rh metal particles supported on the rutile, brookite and the two 10- and 5-nm anatase TiO_2 supports is more easily oxidized upon air exposure (transfer to the XPS chamber) compared with the surface of the Rh metal particles on the TiO_2-ANP support. These electronic property differences are likely the main reasons for the lower activity of the rhodium supported on TiO_2-ANP10 and TiO_2-ANP05 compared with the TiO_2-ANP support (with average particle size of 15 nm). However, the Rh/TiO_2-ANP catalyst also has a higher concentration of hydroxyl groups, particularly the species with an O 1s binding energy of 532 eV, compared with all the other TiO_2 supports, and it is possible that these surface hydroxyl groups influence the reaction.

It is evident from the XPS data that Rh-TiO_2 interactions are structure-dependent, and the electronic properties (oxidation state) of rhodium is not only dependent on the structure of the TiO_2 support (anatase, rutile and brookite), but also on the particle size and the stability of the TiO_2 support and can vary significantly with redox treatments.

4. Conclusions

This study reveals that metal-support interactions in Rh/TiO_2 catalysts are very complex, and this can explain some of the seemingly contradictory conclusions in the literature. To investigate the influence of bulk crystal structure on metal-support interactions, pure phases are very important but are not sufficient as the exposed TiO_2 surface facet, TiO_2 particle size, and active metal particle size (metal loading) also influence these interactions. Under carefully matched conditions, similar average particle sizes (and thus specific surface areas) of anatase, rutile and brookite TiO_2 nanoparticles, and low Rh loading to allow formation of small Rh particles, avoid large differences in metal particle sizes, and maximize metal-support interactions, it is revealed that the interactions between the Rh precursor and the TiO_2 support are dependent on the TiO_2 structure, and also on the TiO_2 particle size. Strong metal support interactions leading to migration of TiO_x over the Rh particles are only observed on anatase and brookite TiO_2 supports, not on the rutile TiO_2 nanoparticles. If geometric SMSIs are observed on rutile TiO_2 supports, it is likely due to an unstable structure (too small particle sizes or unfavorable shapes), which can cause transformations into other TiO_2 phases, as observed in this study for the rutile TiO_2 nanorods. The electronic properties of the supported rhodium species depend sensitively on the TiO_2 structure (phase and particle size) and the reduction conditions. According to XPS, more metallic Rh is present on the Rh/TiO_2-ANP catalyst after reduction at 200 °C compared with all other TiO_2 supports (including the TiO_2-ANP10 and TiO_2-ANP05 supports with smaller anatase particle sizes). This could be the main reason for the higher activity in the propene hydrogenation observed over the Rh/TiO_2-ANP catalyst after reduction at 200 °C. However, this catalyst also has a higher contribution from oxygen species with high binding energy (likely related to hydroxyl groups on the titania support) compared with the other catalysts, which could influence the activity.

In summary, this study reveals that Rh-TiO_2 interactions are dependent not only on the TiO_2 structure, but also the TiO_2 particle size. Therefore, care must be taken to make sure that the desired structure is indeed formed (XRD is not always sufficient for confirmation of the structure), and that the phase and particle size are stable during catalyst synthesis and pretreatment, as well as under reaction conditions.

Acknowledgements

Funding for this work was provided by the National Science Foundation (NSF) CBET grand number 1933723 and NSF Division of Chemistry grant number 2102211. Startup funding from the University of Florida is also gratefully acknowledged. The authors would also like to acknowledge staff at the Research Service Centers at UF. More specifically, we would like to acknowledge Kristy Schepker for training on the XRD instrument, David Hays for collecting XPS data and providing training on the XPS instrument, and Alison Trachet for training on the Raman spectroscopy measurements.

Corresponding Author: Helena Hagelin-Weaver

Notes: The authors declare no competing financial interest.

5. References

[1] T.W. van Deelen, C. Hernández Mejía, K.P. de Jong, Control of metal-support interactions in heterogeneous catalysts to enhance activity and selectivity, Nat. Catal., 2 (2019) 955-970.

[2] A. Sápi, T. Rajkumar, J. Kiss, Á. Kukovecz, Z. Kónya, G.A. Somorjai, Metallic Nanoparticles in Heterogeneous Catalysis, Catal. Lett., 151 (2021) 2153-2175.

[3] H. Zhang, J.F. Banfield, Structural Characteristics and Mechanical and Thermodynamic Properties of Nanocrystalline TiO_2, Chem. Rev., 114 (2014) 9613-9644.

[4] K. Bourikas, C. Kordulis, A. Lycourghiotis, Titanium Dioxide (Anatase and Rutile): Surface Chemistry, Liquid Solid Interface Chemistry, and Scientific Synthesis of Supported Catalysts, Chem. Rev., 114 (2014) 9754-9823.

[5] S.J. Tauster, S.C. Fung, R.L. Garten, Strong Metal-Support Interactions - Group-8 Noble-Metals Supported on TiO_2, J. Am. Chem. Soc., 100 (1978) 170-175.

[6] S.J. Tauster, Strong Metal-Support Interactions, Acc. Chem. Res., 20 (1987) 389-394.

[7] V.V. Zhivonitko, K.V. Kovtunov, I.E. Beck, A.B. Ayupov, V.I. Bukhtiyarov, I.V. Koptyug, Role of Different Active Sites in Heterogeneous Alkene Hydrogenation on Platinum Catalysts Revealed by Means of Parahydrogen-Induced Polarization, J. Phys. Chem. C, 115 (2011) 13386-13391.

[8] A. Di Paola, M. Bellardita, L. Palmisano, Brookite, the Least Known TiO_2 Photocatalyst, Catalysts, 3 (2013) 36-73.

[9] T. Luttrell, S. Halpegamage, J.G. Tao, A. Kramer, E. Sutter, M. Batzill, Why is anatase a better photocatalyst than rutile? - Model studies on epitaxial TiO_2 films, Sci. Rep., 4 (2014).

[10] J.J.M. Vequizo, H. Matsunaga, T. Ishiku, S. Karnimura, T. Ohno, A. Yamakata, Trapping-Induced Enhancement of Photocatalytic Activity on Brookite TiO_2 Powders: Comparison with Anatase and Rutile TiO2 Powders, ACS. Catal., 7 (2017) 2644-2651.

[11] K.-R. Zhu, M.-S. Zhang, J.-M. Hong, Z. Yin, Size effect on phase transition sequence of TiO_2 nanocrystal, Mater. Sci. Eng., A, 403 (2005) 87-93.

[12] A.S. Barnard, L.A. Curtiss, Prediction of TiO_2 Nanoparticle Phase and Shape Transitions Controlled by Surface Chemistry, Nano Lett., 5 (2005) 1261-1266.

[13] A.K.P.D. Savio, J. Fletcher, F.C. Robles Hernández, Sonosynthesis of nanostructured TiO_2 doped with transition metals having variable bandgap, Ceram. Int., 39 (2013) 2753-2765.

[14] M. Tang, S. Li, S. Chen, Y. Ou, M. Hiroaki, W. Yuan, B. Zhu, H. Yang, Y. Gao, Z. Zhang, Y. Wang, Facet-Dependent Oxidative Strong Metal-Support Interactions of Palladium–TiO_2 Determined by In Situ Transmission Electron Microscopy, Angew. Chem. Int. Ed., 60 (2021) 22339-22344.

[15] H. Perron, C. Domain, J. Roques, R. Drot, E. Simoni, H. Catalette, Optimisation of accurate rutile TiO_2 (110), (100), (101) and (001) surface models from periodic DFT calculations, Theor. Chem. Acc., 117 (2007) 565-574.

[16] C.Y. Chang, H.T. Chen, M.C. Lin, Adsorption Configurations and Reactions of Nitric Acid on TiO_2 Rutile (110) and Anatase (101) surfaces, J. Phys. Chem. C, 113 (2009) 6140-6149.

[17] Y. Zhou, D.E. Doronkin, M. Chen, S. Wei, J.-D. Grunwaldt, Interplay of Pt and Crystal Facets of TiO_2: CO Oxidation Activity and Operando XAS/DRIFTS Studies, ACS. Catal., 6 (2016) 7799-7809.

[18] J. Zhang, H. Wang, L. Wang, S. Ali, C.T. Wang, L.X. Wang, X.J. Meng, B. Li, D.S. Su, F.S. Xiao, Wet-Chemistry Strong Metal-Support Interactions in Titania-Supported Au Catalysts, J. Am. Chem. Soc., 141 (2019) 2975-2983.

[19] L. Wang, J. Zhang, Y.H. Zhu, S.D. Xu, C.T. Wang, C.Q. Bian, X.J. Meng, F.S. Xiao, Strong Metal-Support Interactions Achieved by Hydroxide-to-Oxide Support Transformation for Preparation of Sinter-Resistant Gold Nanoparticle Catalysts, ACS. Catal., 7 (2017) 7461-7465.

[20] X.Y. Liu, M.H. Liu, Y.C. Luo, C.Y. Mou, S.D. Lin, H.K. Cheng, J.M. Chen, J.F. Lee, T.S. Lin, Strong Metal-Support Interactions between Gold Nanoparticles and ZnO Nanorods in CO Oxidation, J. Am. Chem. Soc., 134 (2012) 10251-10258.

[21] Y.C. Wang, D. Widmann, R.J. Behm, Influence of TiO_2 Bulk Defects on CO Adsorption and CO Oxidation on Au/TiO_2: Electronic Metal-Support Interactions (EMSIs) in Supported Au Catalysts, ACS. Catal., 7 (2017) 2339-2345.

[22] J.C. Matsubu, S.Y. Zhang, L. DeRita, N.S. Marinkovic, J.G.G. Chen, G.W. Graham, X.Q. Pan, P. Christopher, Adsorbate-mediated strong metal-support interactions in oxide-supported Rh catalysts, Nat. Chem., 9 (2017) 120-127.

[23] C.-J. Pan, M.-C. Tsai, W.-N. Su, J. Rick, N.G. Akalework, A.K. Agegnehu, S.-Y. Cheng, B.-J. Hwang, Tuning/exploiting Strong Metal-Support Interaction (SMSI) in Heterogeneous Catalysis, J. Taiwan Inst. Chem. Eng., 74 (2017) 154-186.

[24] J.P. Belzunegui, J. Sanz, J.M. Rojo, Contribution of physical blocking and electronic effect to establishment of strong metal-support interaction in rhodium/titanium dioxide catalysts, J. Am. Chem. Soc., 114 (1992) 6749-6754.

[25] Z. Luo, G. Zhao, H. Pan, W. Sun, Strong Metal–Support Interaction in Heterogeneous Catalysts, Adv. Energy Mater., 12 2201395.

[26] E. Soszka, M. Jędrzejczyk, C. Lefèvre, D. Ihiawakrim, N. Keller, A.M. Ruppert, TiO_2-supported Co catalysts for the hydrogenation of γ-valerolactone to 2-methyltetrahydrofuran: influence of the support, Catal. Sci. Technol., 12 (2022) 5802-5813.

[27] U. Diebold, The surface science of titanium dioxide, Surf. Sci. Rep., 48 (2003) 53-229.

[28] H. Song, X. Meng, Z.-j. Wang, Z. Wang, H. Chen, Y. Weng, F. Ichihara, M. Oshikiri, T. Kako, J. Ye, Visible-Light-Mediated Methane Activation for Steam Methane Reforming under Mild Conditions: A Case Study of Rh/TiO_2 Catalysts, ACS. Catal., 8 (2018) 7556-7565.

[29] A. Karelovic, P. Ruiz, Mechanistic study of low temperature CO_2 methanation over Rh/TiO_2 catalysts, J. Catal., 301 (2013) 141-153.

[30] A. Erdőhelyi, Hydrogenation of Carbon Dioxide on Supported Rh Catalysts, Catalysts, 10 (2020) 155.

[31] Y. Kohno, T. Yamamoto, T. Tanaka, T. Funabiki, Photoenhanced reduction of CO_2 by H_2 over Rh/TiO_2: Characterization of supported Rh species by means of infrared and X-ray absorption spectroscopy, J. Mol. Catal. A: Chem., 175 (2001) 173-178.

[32] E.V. Pokochueva, D.B. Burueva, L.M. Kovtunova, A.V. Bukhtiyarov, A.Y. Gladky, K.V. Kovtunov, I.V. Koptyug, V.I. Bukhtiyarov, Mechanistic in situ investigation of heterogeneous hydrogenation over Rh/TiO_2 catalysts: selectivity, pairwise route and catalyst nature, Faraday Discuss., 229 (2021) 161-175.

[33] K.V. Kovtunov, D.A. Barskiy, A.M. Coffey, M.L. Truong, O.G. Salnikov, A.K. Khudorozhkov, E.A. Inozemtseva, I.P. Prosvirin, V.I. Bukhtiyarov, K.W. Waddell, E.Y. Chekmenev, I.V. Koptyug, High-resolution 3D proton MRI of hyperpolarized gas enabled by parahydrogen and Rh/TiO_2 heterogeneous catalyst, Chem. Eur. J., 20 (2014) 11636-11639.

[34] O.G. Salnikov, A. Svyatova, L.M. Kovtunova, N.V. Chukanov, V.I. Bukhtiyarov, K.V. Kovtunov, E.Y. Chekmenev, I.V. Koptyug, Heterogeneous Parahydrogen-Induced Polarization of Diethyl Ether for Magnetic Resonance Imaging Applications, Chem. Eur. J., 27 (2021) 1316-1322.

[35] O.G. Salnikov, L.M. Kovtunova, I.V. Skovpin, V.I. Bukhtiyarov, K.V. Kovtunov, I.V. Koptyug, Mechanistic Insight into the Heterogeneous Hydrogenation of Furan Derivatives with the use of Parahydrogen, ChemCatChem, 10 (2018) 1178-1183.

[36] D.A. Barskiy, K.V. Kovtunov, E.Y. Gerasimov, M.A. Phipps, O.G. Salnikov, A.M. Coffey, L.M. Kovtunova, I.P. Prosvirin, V.I. Bukhtiyarov, I.V. Koptyug, E.Y. Chekmenev, 2D Mapping of NMR Signal Enhancement and Relaxation for Heterogeneously Hyperpolarized Propane Gas, J. Phys. Chem. C, 121 (2017) 10038-10046.

[37] D.A. Barskiy, O.G. Salnikov, K.V. Kovtunov, I.V. Koptyug, NMR Signal Enhancement for Hyperpolarized Fluids Continuously Generated in Hydrogenation Reactions with Parahydrogen, J. Phys. Chem. A, 119 (2015) 996-1006.

[38] C. Li, H. Li, L. Zhang, Y. Ma, T. Wang, Hydroformylation of Dicyclopentadiene to Monoformyltricyclodecenes over Supported Ultra-Low Content Rh Catalysts, Prog React Kinet Mec, 43 (2018) 166-172.

[39] H. Chuai, P. Su, H. Liu, B. Zhu, S. Zhang, W. Huang, Alkali and Alkaline Earth Cation-Decorated TiO_2 Nanotube-Supported Rh Catalysts for Vinyl Acetate Hydroformylation, 9 (2019) 194.

[40] M.-L. Kontkanen, M. Tuikka, N.M. Kinnunen, S. Suvanto, M. Haukka, Hydroformylation of 1-Hexene over Rh/Nano-Oxide Catalysts, 3 (2013) 324-337.

[41] Y. Shi, X. Hu, B. Zhu, S. Wang, S. Zhang, W. Huang, Synthesis and characterization of TiO_2 nanotube supported Rh-nanoparticle catalysts for regioselective hydroformylation of vinyl acetate, RSC Advances, 4 (2014) 62215-62222.

[42] A. Cervantes Uribe, G.A. Del Angel Montes, G. Torres-Torres, A. Vázquez-Zavala, F. González-García, A. Cordero-García, R.J.J.o.C.S. Ojeda-López, Correlation of Rh Particle Size with CO Chemisorption: Effect on the Catalytic Oxidation of MTBE, J. Compos. Sci., 3 (2019) 81.

[43] V. Vishwanathan, S. Narayanan, T. Lakshmi, B.J.I.j.o.t. Viswanathan, The influence of preparation methods on strong metal support interaction (SMSI) in Rh/TiO_2 system, Top. Catal., 30 (1992) 104-106.

[44] C. Mateos-Pedrero, S.R. Gonzalez-Carrazan, M.A. Soria, P. Ruiz, Effect of the nature of TiO_2 support over the performances of Rh/TiO_2 catalysts in the partial oxidation of methane, Catal. Today, 203 (2013) 158-162.

[45] R. Zhang, M. Peng, B. Wang, Catalytic selectivity of Rh/TiO_2 catalyst in syngas conversion to ethanol: probing into the mechanism and functions of TiO_2 support and promoter, Catal. Sci. Technol., 7 (2017) 1073-1085.

[46] R. Camposeco, S. Castillo, V. Rodriguez-Gonzalez, M. Hinojosa-Reyes, I. Mejía-Centeno, Tailored TiO_2 nanostructures for supporting Rh_3O_2 and Rh^0 nanoparticles: Enhanced photocatalytic H_2 production, J. Photochem. Photobiol., A, 356 (2018) 92-101.

[47] A.D. Logan, E.J. Braunschweig, A.K. Datye, D.J. Smith, Direct observation of the surfaces of small metal crystallites: rhodium supported on titania, Langmuir, 4 (1988) 827-830.

[48] J.H.A. Martens, R. Prins, H. Zandbergen, D.C. Koningsberger, Structure of Rh/TiO_2 in the Normal and the SMSI State as Determined by Extended X-Ray Absorption Fine-Structure and High-Resolution Transmission Electron-Microscopy, J. Phys. Chem., 92 (1988) 1903-1916.

[49] J.P. Belzunegui, J.M. Rojo, J. Sanz, Proton NMR procedure to estimate the extent of metal surface covered by titanium oxide overlayers in reduced rhodium/titania catalysts, J. Phys. Chem., 95 (1991) 3463-3465.

[50] A.V. Kalinkin, A.V. Pashis, Studies of the effect of strong metal-support interaction (SMSI) over model catalyst Rh/TiO_2, React. Kinet. Catal. Lett., 46 (1992) 33-38.

[51] M.J. Holgado, V. Rives, Ethene Hydrogenation by Rh/TiO_2 under SMSI Conditions, React. Kinet. Catal. Lett., 51 (1993) 319-324.

[52] V. Vishwanathan, S. Narayanan, Evidence for strong metal-support interaction (SMSI) in Rh/TiO_2 system, Catal. Lett., 21 (1993) 183-189.

[53] A. da Costa Faro, C. Kemball, Influence of strong metal–support interaction on exchange with deuterium and other reactions of hydrocarbons. Part 1.—Studies with Rh/TiO_2 and Rh/SiO_2, J. Chem. Soc., Faraday Trans., 91 (1995) 741-748.

[54] C. Linsmeier, H. Knözinger, E. Taglauer, Depth profile analysis of strong metal-support interactions on RhTiO_2 model catalysts, Nucl. Instrum. Methods Phys. Res., Sect. B, 118 (1996) 533-540.

[55] V. Anděra, Investigation of the Rh/TiO_2 system by XPS and XAES, Appl. Surf. Sci., 51 (1991) 1-8.

[56] G. Rupprechter, G. Seeber, H. Goller, K. Hayek, Structure–Activity Correlations on Rh/Al_2O_3 and Rh/TiO_2 Thin Film Model Catalysts after Oxidation and Reduction, J. Catal., 186 (1999) 201-213.

[57] J. Kiss, A. Sápi, M. Tóth, Á. Kukovecz, Z. Kónya, Rh-induced Support Transformation and Rh Incorporation in Titanate Structures and Their Influence on Catalytic Activity, Catalysts, 10 (2020).

[58] C. Linsmeier, E. Taglauer, Strong metal-support interactions on rhodium model catalysts, Appl. Catal., A, 391 (2011) 175-186.

[59] L. Wang, W. Fang, L. Wang, F.-S. Xiao, $NbOPO_4$ Supported Rh Nanoparticles with Strong Metal–Support Interactions for Selective CO_2 Hydrogenation, ChemSusChem, 13 (2020) 6300-6306.

[60] H. Orita, S. Naito, K. Tamaru, Nature of SMSI effect on CO + H_2 reaction over supported rhodium catalysts, J. Phys. Chem., 89 (1985) 3066-3069.

[61] S. Ma, W. Song, B. Liu, H. Zheng, J. Deng, W. Zhong, J. Liu, X.-Q. Gong, Z. Zhao, Elucidation of the high CO_2 reduction selectivity of isolated Rh supported on TiO_2: a DFT study, Catal. Sci. Technol., 6 (2016) 6128-6136.

[62] M.E. Levin, M. Salmeron, A.T. Bell, G.A. Somorjai, The effects of titania and alumina overlayers on the hydrogenation of CO over rhodium, J. Chem. Soc., Faraday Trans. I, 83 (1987) 2061-2069.

[63] O.G. Salnikov, D.B. Burueva, E.Y. Gerasimov, A.V. Bukhtiyarov, A.K. Khudorozhkov, I.P. Prosvirin, L.M. Kovtunova, D.A. Barskiy, V.I. Bukhtiyarov, K.V. Kovtunov, I.V. Koptyug, The effect of oxidative and reductive treatments of titania-supported metal catalysts on the pairwise hydrogen addition to unsaturated hydrocarbons, Catal. Today, 283 (2017) 82-88.

[64] E.W. Zhao, H.B. Zheng, K. Ludden, Y. Xin, H.E. Hagelin-Weaver, C.R. Bowers, Strong Metal-Support Interactions Enhance the Pairwise Selectivity of Parahydrogen Addition over Ir/TiO_2, ACS. Catal., 6 (2016) 974-978.

[65] T. Ekou, L. Ekou, A. Vicente, G. Lafaye, S. Pronier, C. Especel, P. Marécot, Citral hydrogenation over Rh and Pt catalysts supported on TiO_2: Influence of the preparation and activation protocols of the catalysts, J. Mol. Catal. A: Chem., 337 (2011) 82-88.

[66] M.J. Holgado, V. Rives, Hydrogenolysis of light hydrocarbons on Rh/TiO_2. Catalysts reduced at low temperature, React. Kinet. Catal. Lett., 32 (1986) 221-226.

[67] H. Miessner, H. Orita, S. Naito, K. Tamaru, CO hydrogenation on a highly loaded Rh/TiO_2 catalyst and the influence of strong metal-support interaction, React. Kinet. Catal. Lett., 28 (1985) 295-300.

[68] P. Reyes, M.d.C. Aguirre, I. Melián-Cabrera, M. López Granados, J.L.G. Fierro, Crotonaldehyde hydrogenation on Rh/TiO_2 catalysts. In situ DRIFTS studies, Bol. Soc. Chil. Chim., 47 (2002) 547-556.

[69] E.J. Braunschweig, A.D. Logan, A.K. Datye, D.J. Smith, Reversibility of strong metal-support interactions on RhTiO_2, J. Catal., 118 (1989) 227-237.

[70] A. Vicente, T. Ekou, G. Lafaye, C. Especel, P. Marécot, C.T. Williams, Influence of the nature of the precursor salts on the properties of Rh–Ge/TiO_2 catalysts for citral hydrogenation, J. Catal., 275 (2010) 202-210.

[71] O. Dulub, W. Hebenstreit, U. Diebold, Imaging cluster surfaces with atomic resolution: the strong metal-support interaction state of Pt supported on TiO_2(110), Phys. Rev. Lett., 84 (2000) 3646-3649.

[72] X.H. Liu, D. Meng, Y. Deng, Effects of rhodium doping on the microstructures and photocatalytic performances of TiO_2 powders, J. Chem. Res., (2016) 678-682.

[73] L. Yu, K. Sato, T. Toriyama, T. Yamamoto, S. Matsumura, K. Nagaoka, Influence of the Crystal Structure of Titanium Oxide on the Catalytic Activity of Rh/TiO_2 in Steam Reforming of Propane at Low Temperature, Chem-Eur J, 24 (2018) 8742-8746.

[74] A. Yamamoto, J. Ohyama, K. Teramura, T. Shishido, T. Tanaka, Effect of a crystalline phase of TiO_2 photocatalysts on the photodeposition of Rh metal nanoparticles, Catal. Today, 232 (2014) 165-170.

[75] P. Claus, S. Schimpf, R. Schödel, P. Kraak, W. Mörke, D. Hönicke, Hydrogenation of crotonaldehyde on Pt/TiO_2 catalysts: Influence of the phase composition of titania on activity and intramolecular selectivity, Appl. Catal., A, 165 (1997) 429-441.

[76] F. Liu, J. Ftouni, P.C.A. Bruijnincx, B.M. Weckhuysen, Phase-Dependent Stability and Substrate-Induced Deactivation by Strong Metal-Support Interaction of Ru/TiO_2 Catalysts for the Hydrogenation of Levulinic Acid, ChemCatChem, 11 (2019) 2079-2088.

[77] X. Zhang, P. Yan, B. Zhao, K. Liu, M.C. Kung, H.H. Kung, S. Chen, Z.C. Zhang, Selective Hydrodeoxygenation of Guaiacol to Phenolics by Ni/Anatase TiO_2 Catalyst Formed by Cross-Surface Migration of Ni and TiO_2, ACS. Catal., 9 (2019) 3551-3563.

[78] Y.M. Shul'ga, I.N. Ivleva, N.A. Gaidai, T.A. Zav'yalov, E.N. Kurkin, Manifestation of the effect of strong metal-support interaction in a Pt/TiO_2 rutile catalyst, Kinet. Catal., 41 (2000) 231-235.

[79] H. Tang, Y. Su, B. Zhang, A.F. Lee, M.A. Isaacs, K. Wilson, L. Li, Y. Ren, J. Huang, M. Haruta, B. Qiao, X. Liu, C. Jin, D. Su, J. Wang, T. Zhang, Classical strong metal–support interactions between gold nanoparticles and titanium dioxide, Sci. Adv., 3 (2017) e1700231.

[80] O. Ozturk, J.B. Park, S. Ma, J.S. Ratliff, J. Zhou, D.R. Mullins, D.A. Chen, Probing the interactions of Pt, Rh and bimetallic Pt–Rh clusters with the TiO_2(110) support, Surf. Sci., 601 (2007) 3099-3113.

[81] J.B.F. Anderson, R. Burch, J.A. Cairns, The reversibility of strong metal-support interactions. A comparison of Pt/TiO_2 and Rh/TiO_2 catalysts, Appl. Catal., 25 (1986) 173-180.

[82] A. Berkó, I. Ulrych, K.C. Prince, Encapsulation of Rh Nanoparticles Supported on TiO_2(110)-(1×1) Surface: XPS and STM Studies, J. Phys. Chem. B, 102 (1998) 3379-3386.

[83] H.R. Sadeghi, V.E. Henrich, Rh on TiO_2: Model catalyst studies of the strong metal-support interaction, Appl. Surf. Sci., 19 (1984) 330-340.

[84] Y. Li, Y. Zhang, K. Qian, W. Huang, Metal–Support Interactions in Metal/Oxide Catalysts and Oxide–Metal Interactions in Oxide/Metal Inverse Catalysts, ACS. Catal., 12 (2022) 1268-1287.

[85] P. Weerachawanasak, P. Praserthdam, M. Arai, J. Panpranot, A comparative study of strong metal–support interaction and catalytic behavior of Pd catalysts supported on micron- and nano-sized TiO_2 in liquid-phase selective hydrogenation of phenylacetylene, J. Mol. Catal. A: Chem., 279 (2008) 133-139.

[86] Z.F. Wu, Y.Y. Li, W.X. Huang, Size-Dependent Pt-TiO_2 Strong Metal-Support Interaction, J. Phys. Chem. Lett., 11 (2020) 4603-4607.

[87] H.W. Wang, X.K. Gu, X.S. Zheng, H.B. Pan, J.F. Zhu, S. Chen, L.N. Cao, W.X. Li, J.L. Lu, Disentangling the size-dependent geometric and electronic effects of palladium nanocatalysts beyond selectivity, Sci. Adv., 5 (2019).

[88] X. Du, Y. Huang, X. Pan, B. Han, Y. Su, Q. Jiang, M. Li, H. Tang, G. Li, B. Qiao, Size-dependent strong metal-support interaction in TiO_2 supported Au nanocatalysts, Nat. Commun., 11 (2020) 5811.

[89] Y. Zhang, J.X. Liu, K. Qian, A. Jia, D. Li, L. Shi, J. Hu, J. Zhu, W.J.A.C.I.E. Huang, Structure Sensitivity of Au‐TiO_2 Strong Metal‐Support Interactions, Angew. Chem. Int. Ed., 60 (2021) 12074-12081.

[90] B. Han, Y.L. Guo, Y.K. Huang, W. Xi, J. Xu, J. Luo, H.F. Qi, Y.J. Ren, X.Y. Liu, B.T. Qiao, T. Zhang, Strong Metal-Support Interactions between Pt Single Atoms and TiO_2, Angew. Chem. Int. Ed., 59 (2020) 11824-11829.

[91] B. Han, Q. Li, X. Jiang, Y. Guo, Q. Jiang, Y. Su, L. Li, B. Qiao, Switchable Tuning CO_2 Hydrogenation Selectivity by Encapsulation of the Rh Nanoparticles While Exposing Single Atoms, Small, 18 (2022) 2204490.

[92] K. Li, T. Peng, Z. Ying, S. Song, J.J.A.C.B.E. Zhang, Ag-loading on brookite TiO_2 quasi nanocubes with exposed {210} and {001} facets: Activity and selectivity of CO_2 photoreduction to CO/CH_4, 180 (2016) 130-138.

[93] W. Wang, Q. Sun, Q. Wang, S. Li, J. Xu, F. Deng, Heterogeneous parahydrogen induced polarization on Rh-containing silicalite-1 zeolites: effect of the catalyst structure on signal enhancement, Catal. Sci. Technol., 12 (2022) 4442-4449.

[94] D.M. Shakya, O.A. Ejegbavwo, T. Rajeshkumar, S.D. Senanayake, A.J. Brandt, S. Farzandh, N. Acharya, A.M. Ebrahim, A.I. Frenkel, N. Rui, G.L. Tate, J.R. Monnier, K.D. Vogiatzis, N.B. Shustova, D.A. Chen, Selective Catalytic Chemistry at Rhodium(II) Nodes in Bimetallic Metal–Organic Frameworks, Angew. Chem. Int. Ed., 58 (2019) 16533-16537.

[95] W.A. Weber, A. Zhao, B.C. Gates, NaY Zeolite-Supported Rhodium and Iridium Cluster Catalysts: Characterization by X-ray Absorption Spectroscopy during Propene Hydrogenation Catalysis, J. Catal., 182 (1999) 13-29.

[96] G.C. Bond, J.J. Philipson, P.B. Wells, J.M. Winterbottom, Hydrogenation of olefins. Part 3.—Reaction of ethylene and of propylene with deuterium over alumina-supported palladium and rhodium, T Faraday Soc, 62 (1966) 443-454.

[97] F. Pinna, C. Candilera, G. Strukul, M. Bonivento, M. Graziani, Catalytic hydrogenation of propene over polymer supported rhodium complexes, J. Organomet. Chem., 159 (1978) 91-98.

[98] A.L. Marsh, G.A. Somorjai, Structure, reactivity, and mobility of carbonaceous overlayers during olefin hydrogenation on platinum and rhodium single crystal surfaces, Top. Catal., 34 (2005) 121-128.

[99] A.M. Argo, J.F. Odzak, J.F. Goellner, F.S. Lai, F.S. Xiao, B.C. Gates, Catalysis by Oxide-Supported Clusters of Iridium and Rhodium: Hydrogenation of Ethene, Propene, and Toluene, The Journal of Physical Chemistry B, 110 (2006) 1775-1786.

[100] J. Camacho-Bunquin, H. Shou, P. Aich, D.R. Beaulieu, H. Klotzsch, S. Bachman, C.L. Marshall, A. Hock, P. Stair, Catalyst synthesis and evaluation using an integrated atomic layer deposition synthesis–catalysis testing tool, Rev. Sci. Instrum., 86 (2015).

[101] I.V. Koptyug, K.V. Kovtunov, S.R. Burt, M.S. Anwar, C. Hilty, S.-I. Han, A. Pines, R.Z. Sagdeev, para-Hydrogen-Induced Polarization in Heterogeneous Hydrogenation Reactions, J. Am. Chem. Soc., 129 (2007) 5580-5586.

[102] U. Obenaus, S. Lang, R. Himmelmann, M. Hunger, Parahydrogen-Induced Hyperpolarization inside Meso- and Micropores of Pt-, Rh-, Ir-, and Pd-Containing Solid Catalysts, J. Phys. Chem. C, 121 (2017) 9953-9962.

[103] M. Ge, J.W. Li, L. Liu, Z. Zhou, Template-Free Synthesis and Photocatalytic Application of Rutile TiO_2 Hierarchical Nanostructures, Ind. Eng. Chem. Res., 50 (2011) 6681-6687.

[104] J.T. Richardson, Principles of Catalyst Development, Springer New York1989.

[105] I.M.K. Ismail, Cross-sectional areas of adsorbed nitrogen, argon, krypton, and oxygen on carbons and fumed silicas at liquid nitrogen temperature, Langmuir, 8 (1992) 360-365.

[106] B.D. Cullity, S.R. Stock, Elements of X-Ray Diffraction, 3rd Ed., Prentice-Hall Inc.2001, pp. 96-102.

[107] A. Gubbens, M. Barfels, C. Trevor, R. Twesten, P. Mooney, P. Thomas, N. Menon, B. Kraus, C. Mao, B. McGinn, The GIF Quantum, a next generation post-column imaging energy filter, Ultramicroscopy, 110 (2010) 962-970.

[108] J. Verbeeck, S. Van Aert, Model based quantification of EELS spectra, Ultramicroscopy, 101 (2004) 207-224.

[109] R. Door, D. Gängler, Multiple least-squares fitting for quantitative electron energy-loss spectroscopy — an experimental investigation using standard specimens, Ultramicroscopy, 58 (1995) 197-210.

[110] H. Zhang, J.F. Banfield, Understanding Polymorphic Phase Transformation Behavior during Growth of Nanocrystalline Aggregates: Insights from TiO_2, J. Phys. Chem. B, 104 (2000) 3481-3487.

[111] J. Yahui, L. Chunsheng, X. Zhongzhen, L. Wei, G. Daowei, C. Guozhu, The SMSI of Pt-TiO_2 During the Crystalline Phase Transformation and Its Effect on CO Oxidation Performance, Acta Chim. Sinica, 80 (2022) 1289.

[112] Y. Hu, H.L. Tsai, C.L. Huang, Effect of brookite phase on the anatase–rutile transition in titania nanoparticles, J. Eur. Ceram. Soc., 23 (2003) 691-696.

[113] B. Pitna Laskova, L. Kavan, M. Zukalova, K. Mocek, O. Frank, In situ Raman spectroelectrochemistry as a useful tool for detection of TiO_2(anatase) impurities in TiO_2(B) and TiO_2(rutile), Monatshefte für Chemie - Chemical Monthly, 147 (2016) 951-959.

[114] W.F. Zhang, Y.L. He, M.S. Zhang, Z. Yin, Q. Chen, Raman scattering study on anatase TiO_2 nanocrystals, J. Phys. D: Appl. Phys., 33 (2000) 912.

[115] A. Li Bassi, D. Cattaneo, V. Russo, C.E. Bottani, E. Barborini, T. Mazza, P. Piseri, P. Milani, F.O. Ernst, K. Wegner, S.E. Pratsinis, Raman spectroscopy characterization of titania nanoparticles produced by flame pyrolysis: The influence of size and stoichiometry, J. Appl. Phys., 98 (2005).

[116] M.C. Ceballos-Chuc, C.M. Ramos-Castillo, J.J. Alvarado-Gil, G. Oskam, G. Rodríguez-Gattorno, Influence of Brookite Impurities on the Raman Spectrum of TiO_2 Anatase Nanocrystals, J. Phys. Chem. C, 122 (2018) 19921-19930.

[117] R. Belgamwar, R. Verma, T. Das, S. Chakraborty, P. Sarawade, V. Polshettiwar, Defects Tune the Strong Metal–Support Interactions in Copper Supported on Defected Titanium Dioxide Catalysts for CO_2 Reduction, J. Am. Chem. Soc., 145 (2023) 8634-8646.

[118] Y. Wu, Y. Fu, L. Zhang, Y. Ren, X. Chen, B. Yue, H. He, Study of Oxygen Vacancies on Different Facets of Anatase TiO_2, Chin. J. Chem . 37 (2019) 922-928.

[119] F. Bertella, P. Concepción, A. Martínez, The impact of support surface area on the SMSI decoration effect and catalytic performance for Fischer-Tropsch synthesis of Co-Ru/TiO_2-anatase catalysts, Catal. Today, 296 (2017) 170-180.

[120] G. Liu, H.G. Yang, X. Wang, L. Cheng, H. Lu, L. Wang, G.Q. Lu, H.-M. Cheng, Enhanced Photoactivity of Oxygen-Deficient Anatase TiO_2 Sheets with Dominant {001} Facets, J. Phys. Chem. C, 113 (2009) 21784-21788.

[121] F. Tian, Y. Zhang, J. Zhang, C. Pan, Raman Spectroscopy: A New Approach to Measure the Percentage of Anatase TiO_2 Exposed (001) Facets, J. Phys. Chem. C, 116 (2012) 7515-7519.

[122] Y. Zhang, C.X. Harris, P. Wallenmeyer, J. Murowchick, X. Chen, Asymmetric Lattice Vibrational Characteristics of Rutile TiO2 as Revealed by Laser Power Dependent Raman Spectroscopy, J. Phys. Chem. C, 117 (2013) 24015-24022.

[123] V. Swamy, B.C. Muddle, Q.J.A.P.L. Dai, Size-dependent modifications of the Raman spectrum of rutile TiO_2, 89 (2006).

[124] J.C. Parker, R.W. Siegel, Calibration of the Raman spectrum to the oxygen stoichiometry of nanophase TiO_2, Appl. Phys. Lett., 57 (1990) 943-945.

[125] C. Chen, H. Zhang, A.M. Ali, H. Zhang, Correlation Between Tunable Oxygen Defects in TiO_2 Nanoflower and Its Photocatalytic Performance for the Degradation of Organic Waste, 15 (2020) 2050018.

[126] S.A. Abdullah, M.Z. Sahdan, N. Nayan, Z. Embong, C.R.C. Hak, F.J.M.L. Adriyanto, Neutron beam interaction with rutile TiO_2 single crystal (111): Raman and XPS study on Ti^{3+}-oxygen vacancy formation, 263 (2020) 127143.

[127] M.N. Iliev, V.G. Hadjiev, A.P. Litvinchuk, Raman and infrared spectra of brookite (TiO_2): Experiment and theory, Vib. Spectrosc, 64 (2013) 148-152.

[128] G.A. Tompsett, G.A. Bowmaker, R.P. Cooney, J.B. Metson, K.A. Rodgers, J.M. Seakins, The Raman spectrum of brookite, TiO_2 (Pbca, Z = 8), 26 (1995) 57-62.

[129] J. Zhang, S. Yan, L. Fu, F. Wang, M. Yuan, G. Luo, Q. Xu, X. Wang, C. Li, Photocatalytic Degradation of Rhodamine B on Anatase, Rutile, and Brookite TiO_2, Chinese J Catal, 32 (2011) 983-991.

[130] J. Yan, G. Wu, N. Guan, L. Li, Z. Li, X. Cao, Understanding the effect of surface/bulk defects on the photocatalytic activity of TiO_2: anatase versus rutile, PCCP, 15 (2013) 10978-10988.

[131] D. Panayotov, M. Mihaylov, D. Nihtianova, T. Spassov, K. Hadjiivanov, Spectral evidence for hydrogen-induced reversible segregation of CO adsorbed on titania-supported rhodium, PCCP, 16 (2014) 13136-13144.

[132] J. Zhou, Z. Gao, G. Xiang, T. Zhai, Z. Liu, W. Zhao, X. Liang, L. Wang, Interfacial compatibility critically controls Ru/TiO_2 metal-support interaction modes in CO_2 hydrogenation, Nat. Commun., 13 (2022) 327.

[133] F. Cao, N. Gong, Z. Ma, X. Wang, M. Tan, Y. Wu, Y. Tan, Controlling CO_2 hydrogenation selectivity by Rh-based catalysts with different crystalline phases of TiO_2, Chem. Commun., 58 (2022) 4219-4222.

[134] G. Munuera, A.R. Gonzalez-Elipe, J.P. Espinos, J.C. Conesa, J. Soria, J. Sanz, Hydrogen-induced titanium oxide migration onto metallic rhodium in real rhodium/titania catalysts, J. Phys. Chem., 91 (1987) 6625-6628.

[135] S. Sakellson, M. McMillan, G.L. Haller, EXAFS evidence for direct metal-metal bonding in reduced rhodium/titania catalysts, J. Phys. Chem., 90 (1986) 1733-1736.

[136] D. Messou, V. Bernardin, F. Meunier, M.B. Ordoño, A. Urakawa, B.F. Machado, V. Collière, R. Philippe, P. Serp, C. Le Berre, Origin of the synergistic effect between TiO_2 crystalline phases in the Ni/TiO_2-catalyzed CO_2 methanation reaction, J. Catal., 398 (2021) 14-28.

[137] Y.Z. Li, Y.N. Fan, H.P. Yang, B.L. Xu, L.Y. Feng, M.F. Yang, Y. Chen, Strong metal-support interaction and catalytic properties of anatase and rutile supported palladium catalyst Pd/TiO_2, Chem. Phys. Lett., 372 (2003) 160-165.

[138] Y. Li, B. Xu, Y. Fan, N. Feng, A. Qiu, J.M.J. He, H. Yang, Y. Chen, The effect of titania polymorph on the strong metal-support interaction of Pd/TiO_2 catalysts and their application in the liquid phase selective hydrogenation of long chain alkadienes, J. Mol. Catal. A: Chem., 216 (2004) 107-114.

[139] Z.B. Rui, S.R. Wu, C. Peng, H.B. Ji, Comparison of TiO_2 Degussa P25 with anatase and rutile crystalline phases for methane combustion, Chem. Eng. J., 243 (2014) 254-264.

[140] H. Iddir, M.M. Disko, S. Ogut, N.D. Browning, Atomic scale characterization of the Pt/TiO_2 interface, Micron, 36 (2005) 233-241.

[141] J.C. Vis, H.F.J. Van't Buk, T. Huizinga, J. Van Grondelle, R. Prins, Reduction and oxidation of Rh/Al_2O_3 and Rh/TiO_2 catalysts as studied by temperature-programmed reduction and oxidation, J. Mol. Catal., 25 (1984) 367-378.

[142] Y. Liu, G. Ding, G. Zhao, H. She, Y. Zhu, Y. Yang, Conversion of glucose to levulinic acid and upgradation to γ-valerolactone on Ru/TiO_2 catalysts, New J. Chem., 45 (2021) 14406-14413.

[143] H. Van't Blik, J. Van Zon, T. Huizinga, J. Vis, D. Koningsberger, R. Prins, Structure of rhodium in an ultradispersed rhodium/alumina catalyst as studied by EXAFS and other techniques, J. Am. Chem. Soc., 107 (1985) 3139-3147.

[144] Z.L. Zhang, A. Kladi, X.E. Verykios, Structural alterations of highly dispersed Rh/TiO_2 catalyst upon CO adsorption and desorption investigated by infrared spectroscopy, J. Mol. Catal., 89 (1994) 229-246.

[145] Y. Tang, C. Asokan, M.J. Xu, G.W. Graham, X.Q. Pan, P. Christopher, J. Li, P. Sautet, Rh single atoms on TiO_2 dynamically respond to reaction conditions by adapting their site, Nat. Commun., 10 (2019).

[146] H. Iddir, V. Skavysh, S. Öğüt, N.D. Browning, M.M. Disko, Preferential growth of Pt on rutile TiO_2, Physical Review B, 73 (2006) 041403.

[147] G. Gao, Z. Zhao, J. Wang, Y. Xi, P. Sun, F. Li, Boosting chiral carboxylic acid hydrogenation by tuning metal-MOx-support interaction in Pt-ReOx/TiO_2 catalysts, Chinese J Catal, 43 (2022) 2034-2044.

[148] K. Asakura, Y. Iwasawa, H. Kuroda, A new TiO_2-attached rhodium metal catalyst. Catalyst characterization and non-SMSI behaviour, J. Chem. Soc., Faraday Trans. I, 84 (1988) 1329-1340.

[149] M.T. Blasco, J.C. Conesa, J. Soria, A.R. Gonzalez-Elipe, G. Munuera, J.M. Rojo, J. Sanz, Structural changes at the titania surface and their relationship to metal-support interactions in rhodium-titania catalysts, J. Phys. Chem., 92 (1988) 4685-4690.

[150] S. Bernal, F.J. Botana, J.J. Calvino, C. Lopez, J.A. PerezOmil, J.M. Rodriguezlzquierdo, High-resolution electron microscopy investigation of metal-support interactions in Rh/TiO_2, J. Chem. Soc. Faraday T., 92 (1996) 2799-2809.

[151] E. Varga, P. Pusztai, A. Oszko, K. Baan, A. Erdohelyi, Z. Konya, J. Kiss, Stability and Temperature-Induced Agglomeration of Rh Nanoparticles Supported by CeO_2, Langmuir, 32 (2016) 2761-2770.

[152] J. Sanz, J. Rojo, P. Malet, G. Munuera, M. Blasco, J. Conesa, J.J.T.J.o.P.C. Soria, Influence of the hydrogen uptake by the support on metal-support interactions in catalysts. Comparison of the rhodium/titanium dioxide and rhodium/strontium titanate ($SrTiO_3$) systems, J. Phys. Chem., 89 (1985) 5427-5433.

[153] A. Gordeeva, T. Thersleff, Y.-J. Hsu, C. Liebske, P. Ulmer, O. Andersson, U. Häussermann, Electronic structure characterization of TiO_2-II with the α-PbO_2 structure by electron-energy-loss-spectroscopy and comparison with anatase, brookite, and rutile, J. Solid State Chem., 322 (2023) 123952.

[154] R. Brydson, H. Sauer, W. Engel, F. Hofer, Electron energy-loss near-edge structures at the oxygen K edges of titanium(IV) oxygen compounds, J. Phys.: Condens. Matter, 4 (1992) 3429.

[155] R. Brydson, H. Sauer, W. Engel, J.M. Thomass, E. Zeitler, N. Kosugi, H. Kuroda, Electron energy loss and X-ray absorption spectroscopy of rutile and anatase: a test of structural sensitivity, J. Phys.: Condens. Matter, 1 (1989) 797.

[156] NIST X-ray Photoelectron Spectroscopy Database, Version 4.1 (National Institute of Standards and Technology, Gaithersburg, 2012).

[157] L. Óvári, J. Kiss, Growth of Rh nanoclusters on TiO_2(110): XPS and LEIS studies, Appl. Surf. Sci., 252 (2006) 8624-8629.

[158] A. Bueno-López, I. Such-Basáñez, C. Salinas-Martínez de Lecea, Stabilization of active Rh_2O_3 species for catalytic decomposition of N_2O on La-, Pr-doped CeO_2, J. Catal., 244 (2006) 102-112.

[159] M.C. Biesinger, L.W.M. Lau, A.R. Gerson, R.S.C. Smart, Resolving surface chemical states in XPS analysis of first row transition metals, oxides and hydroxides: Sc, Ti, V, Cu and Zn, Appl. Surf. Sci., 257 (2010) 887-898.

[160] P.S. Bagus, C.J. Nelin, C.R. Brundle, S.A. Chambers, A New Mechanism For XPS Line Broadening: The 2p-XPS of Ti(IV), J. Phys. Chem. C, 123 (2019) 7705-7716.

[161] P. Krishnan, M. Liu, P.A. Itty, Z. Liu, V. Rheinheimer, M.-H. Zhang, P.J.M. Monteiro, L.E. Yu, Characterization of photocatalytic TiO_2 powder under varied environments using near ambient pressure X-ray photoelectron spectroscopy, Sci. Rep., 7 (2017) 43298.